Sebastian Rohde, BSc.

Electrochemical investigation of an oxygen and metal extraction method with lunar regolith simulant EAC-1 in a Brønsted acidic ionic liquid.

Master's Thesis

to achieve the university degree of

Diplom-Ingenieur

Master's degree programme: Advanced Materials Science

submitted to

Graz University of Technology

Supervisor

Assoc. Prof. Dr. Bernhard Gollas

Institute for Chemistry and Technology of Materials

In cooperation with

Science Advisor & Spaceship EAC Coordinator at the European Astronaut Centre

Graz, February 1, 2021

Abstract

In this work a novel lunar in-situ resource utilization method was investigated with the goal of assessing the technical process feasibility and its underlying chemical reactions. The concept is based on dissolving regolith in a Brønsted acidic ionic liquid, electrolysing generated water to obtain oxygen and regenerating the ionic liquid by electrochemically replacing all dissolved metal ions in solution with protons initially consumed during dissolution of the regolith. A dissolution procedure was developed using the lunar regolith simulant EAC-1 and the ionic liquid 1-ethyl-3-methylimidazolium hydrogen sulfate. A gravimetric and ICP-OES analysis revealed that up to 31.4±1.5 wt.% of EAC-1 can be dissolved with major fractions of Mg, Fe, Al, Na and Ca ions remaining in solution. The electrochemical properties of the solution were investigated with cyclic voltammetry. The electrochemical potential window of the ionic liquid was found to be at least 2.95 V with hydrogen evolution occurring at the cathodic limit. It was tried without success to regenerate the ionic liquid by electrodepositing metals at the cathode while oxidizing hydrogen at the anode in potential controlled electrolysis experiments. Further cyclic voltammetric studies revealed a temporary passivation of the electrode which is probably due to the precipitation of metal hydroxide onto the cathode surface. This is thought to be caused by the reduction of residual water and the resulting increase of the local pH at the cathode surface. Therefore it is concluded that this method still has fundamental issues arising from the multitude of dissolved ions together with unwanted electrode/electrolyte interactions. In particular the ionic liquid regeneration requires a better understanding of this highly complex medium, before this in-situ resource utilization method can be used successfully.

Kurzfassung

Ziel dieser Arbeit war es die technische Umsetzbarkeit einer neuartigen „in-situ resource utilization“ Methode zur Sauerstoff- bzw. Metall-Gewinnung aus Mondregolith zu überprüfen. Die Funktionsweise der Methode basiert auf drei Schritten. Im ersten Schritt wird Regolith in einer ionischen Flüssigkeit mit Brønsted-Säureeigenschaften gelöst, wobei Wasser entsteht. Anschließend wird das generierte Wasser elektrolysiert und Sauerstoff gewonnen. Letztendlich wird die ionische Flüssigkeit elektrochemisch regeneriert indem Metalle abgeschieden und durch Protonen ersetzt werden, wodurch die Säureeigenschaften der ionischen Flüssigkeit wiederhergestellt werden. Eine Vorgehensweise zur Lösung von Regolith Simulant EAC-1 in 1-Ethyl-3-methylimidazolium hydrogensulfat wurde beschrieben. Gravimetrische und ICP-OES Analyse ergaben, dass sich 31.4+1.5 wt.% des EAC-1 in der ionischen Flüssigkeit gelöst haben. Zusätzlich wurden die Elemente Mg, Fe, Al, Na und Ca in erheblichen Mengen in der Lösung nachgewiesen. Eine elektrochemische Charakterisierung der Lösung mittels cyclischer Voltammetrie wurde durchgeführt und ein elektrochemisches Potentialfenster von mindestens 2.95 V festgestellt. Als limitierende Reaktion am kathodischen Ende des Potentialfensters wurde die Wasserstoffentwicklung identifiziert. Mittels potentialkontrollierter Elektrolysen wurde erfolglos versucht Metalle aus der Lösung abzuscheiden und gleichzeitig Wasserstoff an der Anode zu oxidieren, um dabei die ionische Flüssigkeit zu regenerieren. In weiteren cyclovoltammetrischen Analysen wurde eine temporäre Passivierung der Elektrode festgestellt. Dies wurde vermutlich durch die Reduktion von Restwasser an der Kathode ausgelöst, was zu einer Erhöhung des lokalen pH-Wertes geführt hat, wodurch gelöste Metallionen wahrscheinlich als Metallhydroxide auf der Elektrode ausgefallen sind. Offensichtlich weist diese „in-situ resource utilization“ Methode noch fundamentale Probleme in der technischen Umsetzung auf. Insbesondere für die Regeneration der ionischen Flüssigkeit ist ein besseres Verständnis der Wechselwirkung zwischen Elektrolyt und gelösten Ionen erforderlich.

Contents

Affidavit I
Acknowledgments II
Abbrevations and Symbols III

1 Introduction **1**
1.1 In-situ resource utilization of lunar regolith 1
1.2 Lunar oxygen extraction method using ionic liquids 3

2 Experimental **6**
2.1 Used Chemicals 6
2.2 Dissolution of EAC-1 6
2.3 Removing water from the ionic liquid mixture 8
2.4 Moisture determination (Karl-Fischer) 9
2.5 Preparation of the Ag/Ag^+ reference electrode 9
2.6 Electrochemical glass cell 10
2.7 Electrochemical measurement 12
2.8 ICP-OES sample preparation 13
2.9 Electron microscope sample preparation 13

3 Results and Discussion **14**
3.1 Dissolution of EAC-1 in aqueous $[EMIm][HSO_4]$ 14
3.1.1 Gravimetric analysis 14
3.1.2 Change of pH upon dissolution of EAC-1 16
3.1.3 ICP-OES 19
3.2 Regeneration of the ionic liquid 23
3.2.1 Electrochemical potential window of $[EMIm][HSO_4]$ 23
3.2.2 Cyclic voltammetry of EAC-1 dissolved in $[EMIm][HSO_4]$ 26
3.2.3 Potential controlled electrolysis experiments 29
3.2.4 Fe(III) addition experiment 34
3.2.5 Characteristics of Fe(III) in $[EMIm][HSO_4]$ 37
3.2.6 Characteristics of Fe(II) in $[EMIm][HSO_4]$ 42
3.2.7 Electrochemical behavior of dissolved Fe(III) in $[EMIm][HSO_4]$ of varying acidity 43

4 Conclusion **47**
Bibliography 49

List of Figures 52
List of Tables 54
Appendix 56

Affidavit

I declare that I have authored this thesis independently, that I have not used other than the declared sources/resources, and that I have explicitly indicated all material which has been quoted either literally or by content from the sources used. The text document uploaded to tugrazonline is identical to the present master‘s thesis.

Date	Signature

Acknowledgments

I would like to express my gratitude to Prof. Bernhard Gollas, who guided me throughout the complex world of electrochemistry and for his scientific supervision and support. I would also like to extend my deepest appreciation to Dr. Aidan Cowley from the European Space Agency, who inspired me to devote my time towards space sciences and for his generous support and encouragement. I would like to acknowledge the help of Dr. Fernando Warchomicka and Dr. Helmar Wiltsche for assisting me with my experiments. Finally, I would particularly like to thank my parents, Eva and Thorsten, for always supporting me in my endeavors and enabling me to study and learn about things I could never have imagined.

Figure 1: Picture of the moon as seen from earth. Dark patches are the mare regions, brighter areas are the highland regions (Photo by Mike Petrucci on Unspash).

1 Introduction

1.1 In-situ resource utilization of lunar regolith

In-situ resource utilization (ISRU) is going to play a major role in enabling the upcoming expansion of human presence and habitation in space. The fundamental idea of ISRU is to use existing resources in space, like lunar regolith, to produce essential supplies on the spot instead of relying upon earth based deliveries. Besides water, also oxygen will be of key importance, since it can be utilized as rocket fuel and for life support.
During the Apollo missions a total of 382 kg lunar material was collected by astronauts at various landing sites [1]. Also the Russian Luna missions collected a total of 301 g lunar material with their automated landers [2–4]. Recently, the Chinese National Space Administration (CNSA) landed on the moon on December 1, 2020 and returned 1731 g of lunar regolith back to earth. All returned samples were extensively analyzed and together with satellite data a substantial understanding of the lunar material was obtained. In

Table 1: Oxide fractions in lunar regolith types [8] and EAC-1 simulant [7]. EAC-1 was analyzed with EDX and only fractions ≥ 0.5 wt.% are displayed.

	Highland	**Low Ti mare**	**High Ti mare**	**EAC-1**
SiO_2 [wt.%]	44.9	45.1	41.0	43.9
FeO [wt.%]	6.2	17.0	16.6	13.8
Al_2O_3 [wt.%]	25.1	13.1	12.4	10.8
CaO [wt.%]	14.9	10.7	11.4	10.8
MgO [wt.%]	7.5	9.9	8.9	12.6
TiO_2 [wt.%]	0.5	2.9	8.5	2.3
Na_2O [wt.%]	0.4	0.4	0.4	3.6
K_2O [wt.%]	0.1	0.2	0.1	1.1
P_4O_{10} [wt.%]	0.1	0.2	0.1	0.7

general, lunar regolith can be broadly differentiated into three classes: high or low titanium lunar mare and lunar highland regolith. The mare regions, which are the darker patches of the lunar landscape as seen in Figure 1, consist mainly of basaltic lava flow in impact basins, while the brighter highland regions are composed of impact-shocked rock as described by Schreiner et al. [5]. All regolith types are a mixture of minerals namely plagioclase, olivin, pyroxene and ilmenite. By weight, lunar regolith consists of 40-45 wt.% oxygen, which makes oxygen the most abundant element on the lunar surface. Since ISRU experiments are inherently destructive procedures, most experiments cannot be conducted with the precious lunar samples. Thus an adequate simulant material is required and various lunar simulants have been developed for different use-cases [6]. Recently, a novel lunar regolith simulant EAC-1 has been developed for the European Astronaut Centre (EAC), sharing similar physical characteristics most comparable to the Apollo 17 samples [7]. An overview of the respective oxide fractions in lunar regolith types and EAC-1 simulant is given in Table 1.
Several different extraction methods have been investigated for the separation of chemically bound oxygen from regolith and are reviewed by Taylor and Carrier as well as Schlüter and Cowley [9, 10]. Most of the approaches can be summarized in three main concepts:

- Reactive gas-based extraction, using gases like H_2, CH_4 or F_2
- Vacuum pyrolysis-based extraction
- Electrolysis-based extraction

The reactive gas approach aims to replace bound oxygen either by substitution or via reduction of the metal. A well investigated reactive gas approach is the regolith high

temperature reduction with hydrogen gas, leading to the formation of H_2O. Oxygen is produced by electrolyzing formed water while the hydrogen is reused. Gibson et al.[11] performed this method on an actual lunar sample (lunar basalt 70035) achieving an oxygen yield of 2.93 to 4.61 wt.%. This relatively low yield is explained due to the fact that only the iron containing fraction, e.g. ilmenite ($FeTiO_3$), can be reduced with hydrogen. Owing to its simplicity, this method is one of the main oxygen extraction candidates that are being considered [12], even though a higher oxygen yield would certainly be desirable.
In the vacuum pyrolysis method regolith is heated to temperatures far exceeding 1000 °C under high vacuum conditions, which leads to the spontaneous dissociation of oxides into sub-oxides, metals and oxygen [13]. An advantage of the vacuum pyrolysis over other processes is that it utilizes all regolith fractions, thus a previous beneficiation of regolith is not required. A further advantage is that no consumables are needed in the process and the main requirements are heat and vacuum, which are abundant in space if focused sunlight is used. While this is a quite simple approach, many problems arise from the extreme temperatures needed and the separation of formed sub-oxides from oxygen.
Finally, processes using electrolysis to extract oxygen form regolith have been investigated, where oxygen ions are oxidised at the anode and metal ions are reduced at the cathode. In order to increase ion mobility, regolith has to be either molten or dissolved in an appropriate electrolyte. The melting temperature of lunar regolith is in the range of 1100-1380 °C [14] (depending on its composition), making it hard to find suitable electrode materials stable in these conditions. Thus, processes using $CaCl_2$ as an electrolyte like the FFC-Cambridge process [15] have been of great interest, since a high oxygen ion mobility can be maintained even at temperatures as low as 900 °C. Another advantage of the electrolysis approach is that in theory an oxygen yield of 100 % can be achieved and metals are formed as a side product, adding an additional resource. While advances made in this field seem promising, an operating temperature in the range of 900 °C is still very high, and a suitable long duration anode material has yet to be found.

1.2 Lunar oxygen extraction method using ionic liquids

A novel oxygen extraction approach aims to benefit from the properties of ionic liquids (ILs) in an electrolysis process. Due to their extremely low vapor pressures, potential re-usability, non-toxicity, non-flammability and large electrochemical potential window, ILs represent well suited electrolyte candidates in the lunar environment.
Many well known reviews cover the history, synthesis routes and chemical properties of ILs [16, 17]. The term 'ionic liquid' was coined to describe salts with a melting temperature below the boiling point of water, separating ILs from conventional inorganic molten salts

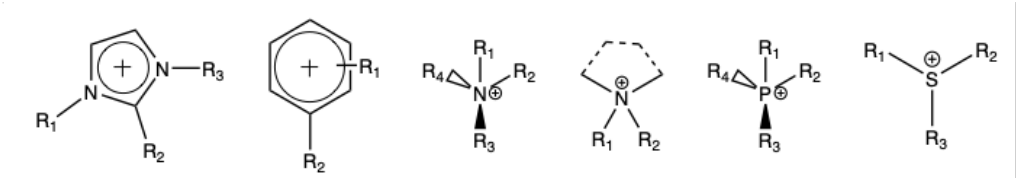

Figure 2: Examples of commonly used cation structures for the synthesis of ionic liquids. [18]

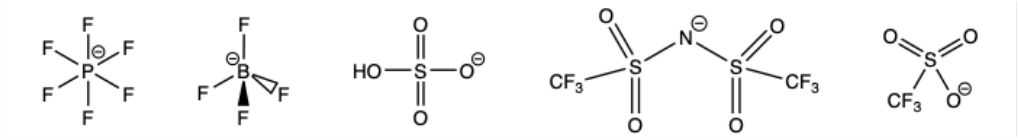

Figure 3: Examples of commonly used anions for the synthesis of ionic liquids. [18]

only by their temperature. While this is a rather vague definition, most ILs interestingly have very similar structures consisting of an organic cation and an inorganic anion. Thus the synthesis of ILs can be split into two steps, the formation of organic cations and an anion exchange reaction delivering the desired anion. The high variability of the ions, especially of the organic cations, and the reams of possible anion and cation combinations (Figure 2 and 3), result in a large number of available ILs and it is relatively straight forward to discoverer new species with novel properties. This lead to an explosion of publications in this field over the last two decades, with ILs now being used in analysis, biocatalysis, electrochemical devices, or as engineering fluids [17].

In the 2009 Space, Propulsion and Energy Sciences International Forum, Paley et al. [19] suggested a process using protic acidic ILs to dissolve regolith and extract oxygen via electrolysis. Recently, Karr et al. continued to investigate this approach and summarised their findings in a technical report [20].

The reported process can be split up into three steps. First the protic acidic IL is used to dissolve metal oxides in regolith. This can be achieved by using an IL like [EMIm][HSO_4] (Figure 4) with an hydrogen sulfate anion, where the proton acts as an Brønsted acid (Equation 1). The dissolution can be accelerated by mixing the IL with water which acts as a ligand by coordinating to the metallic ions in the solution [19], and heating the mixture to moderate temperatures of around 100 °C.

$$\mathrm{MO(s)} + 2\,\mathrm{HSO_4}^- \longrightarrow \mathrm{M}^{2+}\mathrm{(l)} + 2\,\mathrm{SO_4}^{2-} + \mathrm{H_2O} \tag{1}$$

Following regolith dissolution, the water is electrolysed yielding hydrogen and oxygen as seen in Equation 2. This can be done either directly in the ionic liquid mixture or

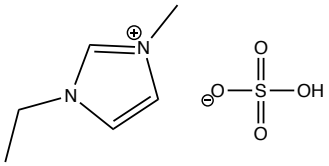

Figure 4: Chemical structure of the protic acidic ionic liquid 1-ethyl-3-methylimidazolium hydrogen sulfate ([EMIm][HSO_4]) as used in this work and by Karr et al. [20]

after separation of the water by distillation and conducting the electrolysis in a different reactor.

$$2\,H_2O(l) \longrightarrow 2\,H_2(g) + O_2(g) \tag{2}$$

The decisive final step is to regenerate the proton depleted IL by oxidising hydrogen gas at the anode while simultaneously electroplating dissolved metals at the cathode (Equations 3 and 4). In the technical report, it is suggested to use a (platinized) platinum anode, to catalyse the hydrogen oxidation.

$$H_2(g) + 2\,{SO_4}^{2-} \xrightarrow{\text{Pt. Anode}} 2\,{HSO_4}^{-}(l) + 2\,e^- \tag{3}$$

$$M^{2+}(l) + 2\,e^- \xrightarrow{\text{Cathode}} M(s) \tag{4}$$

The authors claim that no IL is consumed and the process could be repeated indefinitely as long as there is regolith input and an energy source, yet a precise experimental description of the regeneration step is not given. The only experimental indication that a re-protonation of H^+ depleted ILs can be achieved, was given in the 2009 conference presentation [19]. In these experiments the IL was run through a proton exchange column, achieving 97 % of regenerated IL by weight, and subsequently the dissolution experiments were successfully repeated for a total of four times.
This work aims to implement the oxygen extraction method suggested by Karr et al. using an EAC-1 lunar regolith simulant. First, the dissolution behavior of regolith in the ionic liquid will be studied with simple gravimetric measurements, while the dissolved metal species are analyzed by ICP-OES. After the dissolution, emphasis will be put on reviewing the regeneration step, proving its viability and shedding light on the metal ion reduction behavior in the ionic liquid.

2 Experimental

2.1 Used Chemicals

All chemicals used in this work, their application, CAS-number and supplier are listed in Table 2.

Table 2: List of all chemicals used in this work

Name	Comment	CAS	Supplier
1-Ethyl-3-Methylimidazolium hydrogen sulfate, 98%	Protic acidic ionic liquid used to dissolve regolith	412009-61-1	proionic GmbH, Raaba-Grambach (AUT)
EAC-1	Lunar regolith simulant [7]	-	European Astronaut Centre, Cologne (GER)
Silver nitrate, 99.0%	Silver salt for Ag/Ag+ reference electrode solution	7761- 88-8	Alfa Aesar, Kandel (GER)
Acetonitrile, 99.8%	Solvent for Ag/Ag+ reference electrode solution	75-05-8	Sigma Aldrich, St. Louis (USA)
Tetrabutylammonium perchlorate, electrochemical grade	Conduction salt for Ag/Ag+ reference electrode solution	1923-70-2	Sigma Aldrich (Fluka), St. Louis (USA)
Iron(III)sulfate, 97%	Used for controlled Fe(III) addition	15244-10-7	Sigma Aldrich, St. Louis (USA)
Iron(II)sulfate $\cdot xH_2O$, 99%	Used for controlled Fe(II) addition	13463-43-9	Sigma Aldrich, St. Louis (USA)

2.2 Dissolution of EAC-1

Before any experiments were conducted, the EAC-1 simulant was dried at 100 °C for 24 h in a Memmert drying oven to remove absorbed water and gases.

Table 3: Parameters of dissolution experiments based on 1 g of EAC-1 regolith simulant material.

Regolith mass [g]	Ionic liquid mass [g]	De-ionized H_2O Volume [ml]	Temperature [°C]	Duration [h]
1	0 - 10	30	120	24

A defined amount of EAC-1 was weighed with a high precision scale and filled into a 500 ml round bottom flask. A set amount of ionic liquid and water were added into the glass flask, which was subsequently connected to a reflux condenser and heated using a silicone oil bath. The whole glass assembly was placed onto a magnet stirrer with a heating plate as it can be seen in Figure 5. The oil bath temperature was controlled with a thermocouple and set to be 120 °C. The mixture was heated under reflux for 24 hours. The pH-value of this aqueous suspension was measured before and after the dissolution step with a pH-meter (Schott pH-Meter CG 804).

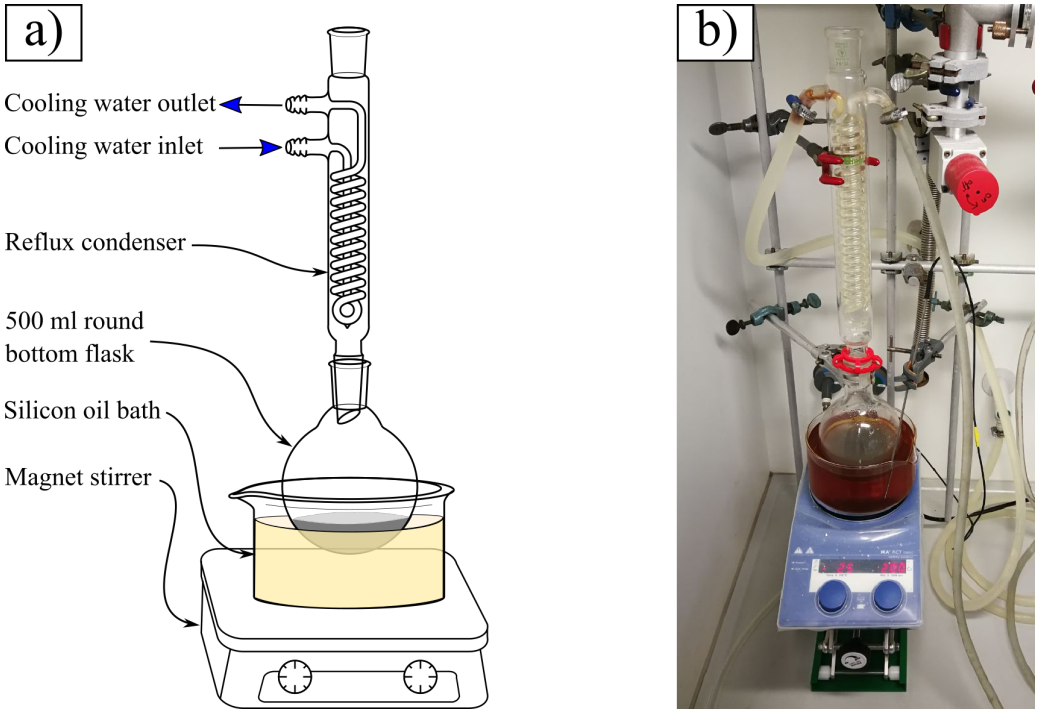

Figure 5: (a) Drawing illustrating the experimental setup for EAC-1 dissolution; (b) picture of the EAC-1 dissolution setup.

This dissolution step did not dissolve all regolith, hence the suspension was filtered to remove the remaining undissolved regolith simulant material. A vacuum filtration unit (Figure 6) equipped with a POR 3 / G 3 ceramic glass frit was used. The regolith residue in the glass frit was washed with de-ionized water to quantitatively transfer all of the

ionic liquid, which might still adhere to the mineral mix, to the filtrate solution.

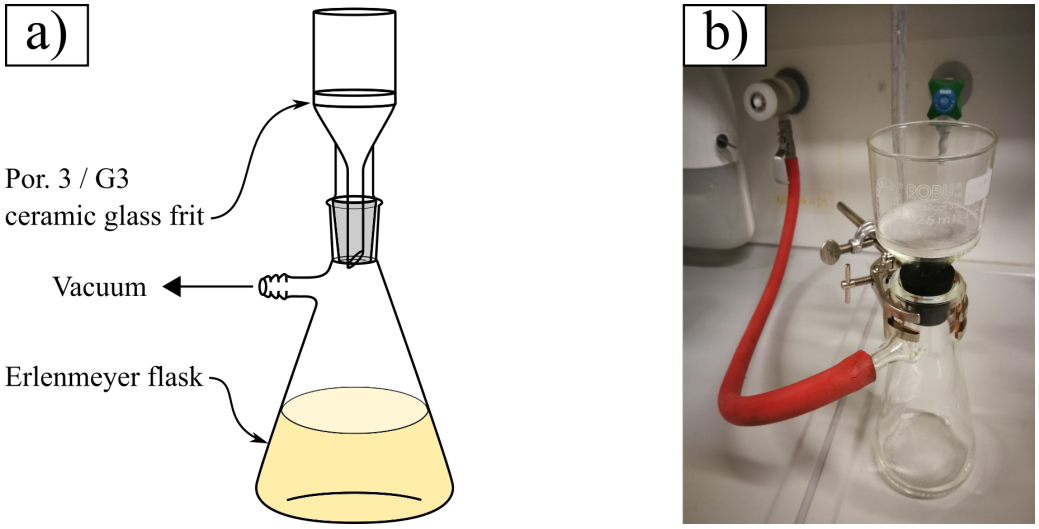

Figure 6: (a) Drawing illustrating the vacuum filtration setup; (b) picture of the vacuum filtration setup.

2.3 Removing water from the ionic liquid mixture

The remaining filtrate from the dissolution step was a mixture of ionic liquid, water, and dissolved metal ions. For the following electrochemical investigation water had to be removed because it decreases the electrochemical potential window. Therefore the solution was pre-dried at 120 °C using the same setup as for the dissolution step (Figure 5), yet this time without the reflux condenser. This step, which was usually carried out overnight, was implemented until the total volume of the solution had decreased significantly and no evaporation was evident anymore.

Finally, the pre-dried ionic liquid mixture was transferred into the electrochemical glass cell. In order to remove all remaining water as completely as possible, a vacuum of 3 to $5 \cdot 10^{-2}$ mbar was applied, and the glass cell was heated to 70°C using a thermostat (Figure 7). These conditions were held until visible boiling of the solution stopped, which was usually achieved within five hours.

Figure 7: Picture of the setup used to dry the ionic liquid mixture. In this picture a glass cell and a round bottom flask are connected to the vacuum line. The glass cell is heated with a thermostat, the round bottom flask with an oil bath.

2.4 Moisture determination (Karl-Fischer)

The water content of the dried substances was determined by the Karl-Fischer method using a Misubishi (Japan) "Moisturemeter" model CA-100 / VA-100.

2.5 Preparation of the Ag/Ag^+ reference electrode

For the electrochemical investigation a Ag/Ag^+ reference electrode was chosen, which is a commonly used reference electrode in non aqueous systems and ionic liquids [21]. In order to ensure that the entire reference electrode/Luggin capillary setup remained water free, it was assembled in a glovebox under a 5.0 argon atmosphere. The setup consists of a silver wire immersed into a 0.01 M solution of silver nitrate/0.1 M tetrabutylammonium perchlorate in anhydrous acetonitrile contained in a glass frit, which is inserted via an intermediate glass frit filled with dry IL into the IL-filled Haber-Luggin capillary (Figure 8). The intermediate glass frit is used to circumvent incompatibilities between the liquids in the reference electrode and the electrolyte in the capillary. The intermediate glass frit as well as the Haber-Luggin capillary were filled with dried [EMIm][HSO_4] (water content: $<$5 ppm), since no incompatibilities between the silver-ion solution and the IL were ex-

pected. The silver-ion solution was renewed for each new setup of the electrochemical cell to avoid degeneration. Additionally, the electrode was protected from uv light with aluminum foil.

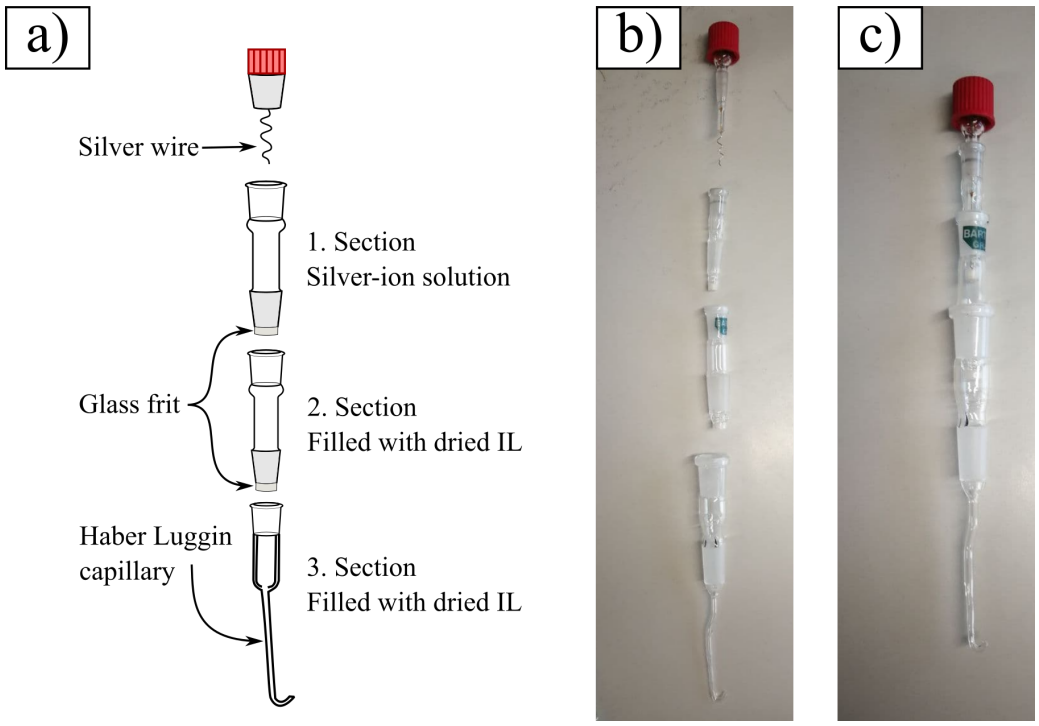

Figure 8: (a) Drawing illustrating the glass Haber Luggin capillary reference electrode setup; (b) Picture of disassembled reference electrode; (c) picture of assembled reference electrode.

2.6 Electrochemical glass cell

The electrochemical glass cell was equipped with five ISO 14/23 standard ground joints in which the electrodes and other equipment can be inserted. The measurement chamber is surrounded by a thermostating mantle, which allows precise temperature control with a thermofluid from a thermostat as demonstrated in Figure 9. For the measurement, the cell is equipped with a working electrode of different electrode materials (usually a 3 mm diameter glassy carbon disk-electrode from Metrohm), a Pt mesh counter electrode, the Ag/Ag^+ reference electrode, a gas inlet with a bubbler and a thermometer (Figure 10). Additionally, a small magnetic stir bar is added to stir the solution in-between measurements.

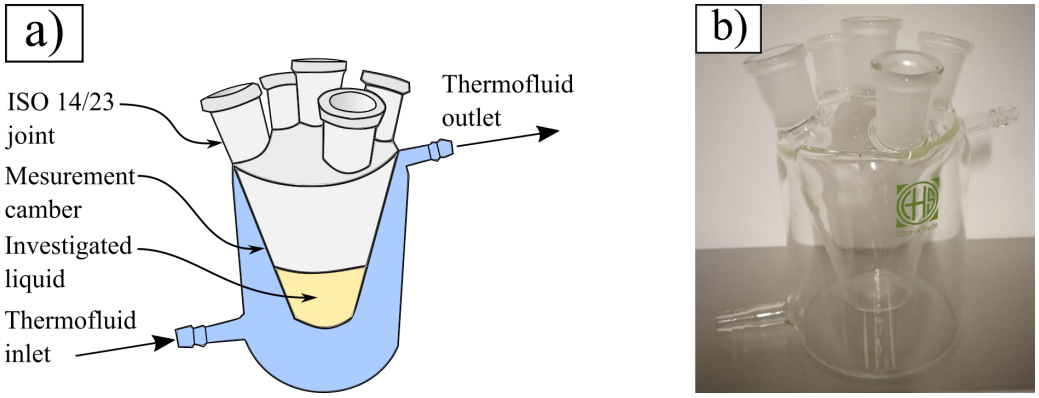

Figure 9: (a) Drawing of the electrochemical glass cell; (b) picture of an empty electrochemical glass cell.

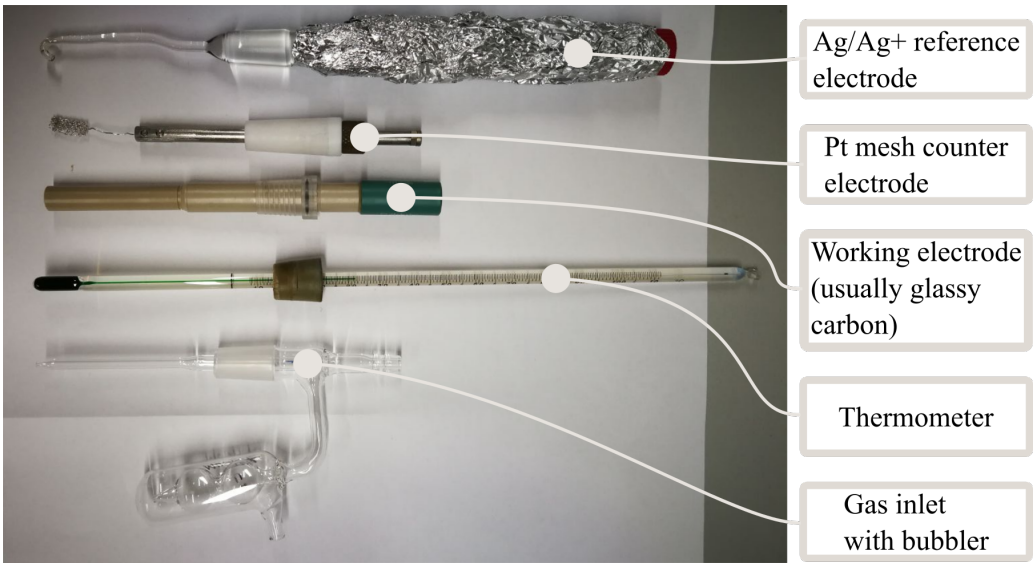

Figure 10: Typical electrochemical equipment, which is inserted into the 5-joint glass cell

As soon as all the equipment is placed into the glass cell, the Haber Luggin capillary of the reference electrode is rotated in the cell until its open capillary end is placed about 1-2 mm away from the round disk working electrode (Figure 11), to accurately control the working electrode potential.

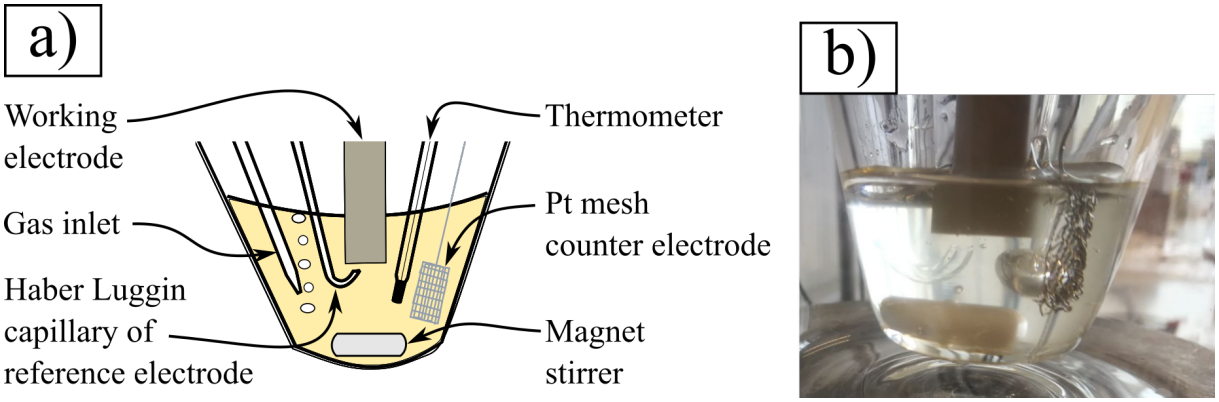

Figure 11: (a) Drawing illustrating a close up view of the electrode arrangement inside the glass cell filled with electrolyte; (b) close-up picture of the electrode arrangement in the electrochemical glass cell.

2.7 Electrochemical measurement

Before each measurement, the working electrode was polished with 0.3 µm aluminum oxide powder and the solution was purged for at least 15 minutes with nitrogen or 5.0 hydrogen gas, removing dissolved oxygen. Hydrogen was used in long lasting potential controlled electrolysis measurements to supply a reactant to the counter electrode, which can be oxidized instead of the electrolyte. The glass cell was thermostated to 70 °C increasing the ion mobility of the viscous solution. Cyclic voltammetry as well as chrono-amperometry was conducted with a Metrohm Autolab B.V. PGSTAT302N. All measurements were carried out inside a Faraday cage, shielded from external electromagnetic interference. An overview of the experimental setup can be seen in Figure 12. All data was recorded and analyzed with the Metrohm NOVA 1.11 software.

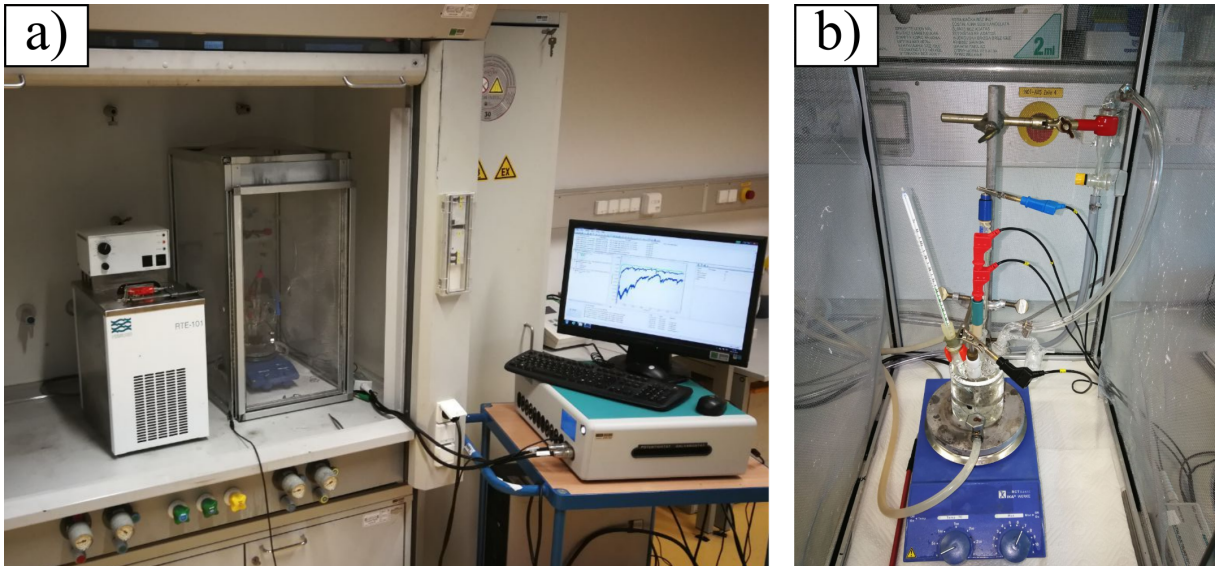

Figure 12: (a) Picture showing the measurement setup inside a fume hood; (b) Close up picture of the electrochemical glass cell inside the faraday cage connected to the potentiostat.

2.8 ICP-OES sample preparation

In order to determine which metal species can be dissolved with the previously explained dissolution procedure, an ICP-OES[1] was conducted. 4 ml samples were taken from the aqueous IL solution directly after the vacuum filtration step. They were additionally filtered with 1.0 µm disposable syringe filters. Ideally the samples would be taken from the dried and concentrated IL mixture, yet this solution turned out to be too viscous to be filtered and therefore couldn't be investigated with the ICP-OES device. Since no precipitation was observed in the dried IL solution, all measured metal species in the aqueous solution were assumed be present in the dried solution too.

2.9 Electron microscope sample preparation

In order to detect metal deposits on electrode surfaces, electrodes were investigated with a field emission scanning electron microscope[2] (SEM) from TESCAN MIRA3 (TESCAN Brno s.r.o., Brno, Czech Republic) equipped with an X-ray spectrometer and an Octane Plus detector to conduct energy dispersive X-ray spectroscopy (EDX). The TEAM v.4.5

[1] Thanks to Wiltsche, Helmar, Dipl.-Ing. Dr.techn. at the Institute of Analytical Chemistry and Food Chemistry for conducting all ICP-OES measurements. All ICP-OES data is listed in the appendix (Table A2).

[2] Thanks to Warchomicka, Fernando Gustavo, Dr.techn. at the Institute of Materials Science, Joining and Forming for conducting all electron microscopy and EDX measurements.

software (Ametek, Inc. Berwyn, PA, USA) was used to analyze the data.
The electrode samples were created using a PINE research instrumentation E6 Series "Change Disk" rotating ring-disk electrode set, which had the option to exchange or remove the disk electrode from the assembly. After the chronoamperometry experiment, a few selected electrode samples (see Section 3.2.3) were removed from the PINE electrode and stored under air. Within one week after sample preparation, the electrodes were placed onto a sample holder and investigated with the electron microscope.

3 Results and Discussion

3.1 Dissolution of EAC-1 in aqueous [EMIm][HSO_4]

3.1.1 Gravimetric analysis

By measuring the weight difference of EAC-1 before and after the dissolution step in relation to the amount of IL, the dissolution percentage was measured and is shown in Figure 13. Where 7 grams of [EMIm][HSO_4] were added to one gram of EAC-1 there were three dissolution experiments conducted. These measurements have different dissolution percentages ranging from 30 wt.% to 33 wt.%. This inaccuracy of about ± 1.5 wt.% has to be assumed for each measurement point. That error probably originates from the inaccuracy of the scale or different particle sizes in the EAC-1 regolith simulant material, which might have led to different dissolution rates.

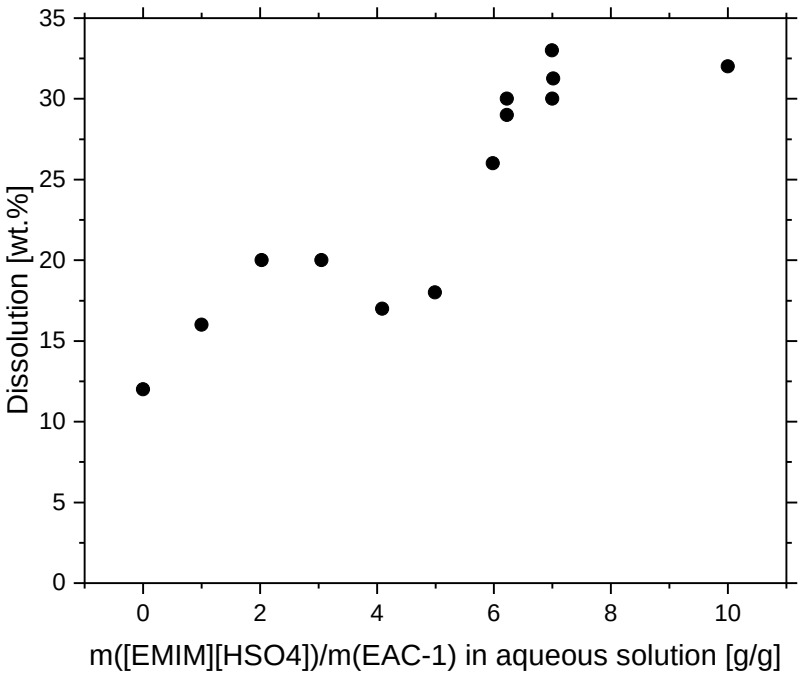

Figure 13: Graph relating the dissolved fraction of EAC-1 to the amount of IL added to 30 ml water.

One can see that even without adding any [EMIm][HSO$_4$] to the mixture, already 12 wt.% of EAC-1 dissolves. This is due to the reaction of water soluble compounds CaO [22], Na_2O [23], K_2O [24] and P_4O_{10} [25] in EAC-1. These compounds can either react acidic or basic as shown in Equations 5, 6, 7 and 8.

$$CaO + H_2O \longrightarrow Ca^{2+} + 2\,OH^- \tag{5}$$

$$Na_2O + H_2O \longrightarrow 2\,Na^+ + 2\,OH^- \tag{6}$$

$$K_2O + H_2O \longrightarrow 2\,K^+ + 2\,OH^- \tag{7}$$

$$P_4O_{10} + 6\,H_2O \longrightarrow 12\,H^+ + 4\,PO_4{}^{3-} \tag{8}$$

This leads to a high variety of different dissolved metal species, each of them individually influencing the pH value. Large amounts of different ion species in solution can also cause additional complications. The reaction of $PO_4{}^{3-}$ with Ca^{2+} for example, leads to highly

insoluble calcium phosphate while the reaction of Ca^{2+} with IL and water could lead to the formation of gypsum. These reactions of dissolved ions with each other demonstrate the high complexity of the solution.
According to Table 1 all water soluble chemicals together account for 16.2 wt.% of the total weight of EAC-1. Considering the measuring inaccuracy, about 65 wt.% to 84 wt.% of water soluble components were dissolved. The undissolved fractions of water soluble components might be enclosed in larger particles.
As soon as [EMIm][HSO_4] is added to the mixture, the dissolution efficiency increases to around 20 wt.% until it further increases to about 30 wt.% when an excess of 6 g IL of is used. It seems that by further increasing the ionic liquid amount to 10 grams per gram of regolith simulant did not increase the dissolved fraction. Thus a maximum relative dissolution of 31.4±1.5 wt.% is reported when 7 g of [EMIm][HSO_4] or more are used per gram of EAC-1. Hence, every time the EAC-1 solution is mentioned in this work, a concentration of 7 g IL per one gram of EAC-1 regolith simulant was used, if not noted otherwise.
A table summarizing all dissolution efficiencies and pH changes can be found in the appendix (Table A1).

3.1.2 Change of pH upon dissolution of EAC-1

As described in Section 2.2, the pH was measured directly in the regolith suspension before and after the dissolution procedure. Additionally, the pH before the dissolution reaction was calculated. The calculation is based on the dissociation reaction of HSO_4^- according to Equation 9.

$$HSO_4^- + H_2O \longrightarrow H_3O^+ + SO_4^{2-} \tag{9}$$

From this equation the dissociation constant K can be derived as follows:

$$K = \frac{c(H_3O^+) \cdot c(SO_4^{2-})}{c(HSO_4^-)} \tag{10}$$

Since water is abundant in excess, it is not considered for the calculation of K. In equilibrium, the concentration c of the anion $c(HSO_4^-)$ is equal to the initial concentration c_0 minus the concentration of protons $c(H_3O^+)$ and the proton concentration must be equal to $c(SO_4^{2-})$. This leads to a simplification of the dissociation constant according to

Equation 11.

$$K = \frac{(c(\mathrm{H_3O^+}))^2}{c_0 - c(\mathrm{H_3O^+})} \tag{11}$$

Using this equation, the proton concentration can be derived, which directly relates to the pH value as shown in Equations 12 and 13.

$$c(\mathrm{H_3O^+}) = -K/2 + \sqrt{(K/2)^2 + K \cdot c_0} \tag{12}$$

$$pH = -log(c(\mathrm{H_3O^+})) \tag{13}$$

The acid constant pKa for HSO_4^- is 1.99 [26], which represents a dissociation constant K of 0.0102. For [EMIm][HSO_4] a density of 1.367 g/ml was used as specified by the supplier (Figure A2). The pH value was calculated for each IL concentration step as seen in Table 4.

Table 4: Data used to calculate the pH value of the aqueous suspension before the dissolution of EAC-1.

Mass of added IL [g]	Volume [ml]	c(H_3O^+) [M]	calculated pH
1	30.7	0.156	1.45
2	31.5	0.305	1.29
3	32.2	0.448	1.20
4	32.9	0.583	1.14
5	33.7	0.714	1.09
6	34.4	0.838	1.06
7	35.1	0.957	1.03

Additionally, it was tried to correlate the acidity of the aqueous ionic liquid mixture directly to the solubility of EAC-1 by plotting the dissolution values versus the pH value (Figure A1). From that Figure one can obtain that a higher dissolution of above 25 wt.% was only possible in pH regions with values lower than 1.15. Yet in some measurements also smaller amounts of EAC-1 were dissolved in these low pH regions. The absence of a clear correlation between the pH and gravimetric dissolution data indicates that water soluble components of EAC-1 were already (partially) dissolved during the measurement and thus interfered with the pH. To get a precise correlation of the acidity with total dissolution, more experimental data is required and the pH needs to be measured before EAC-1 is added to the mixture.

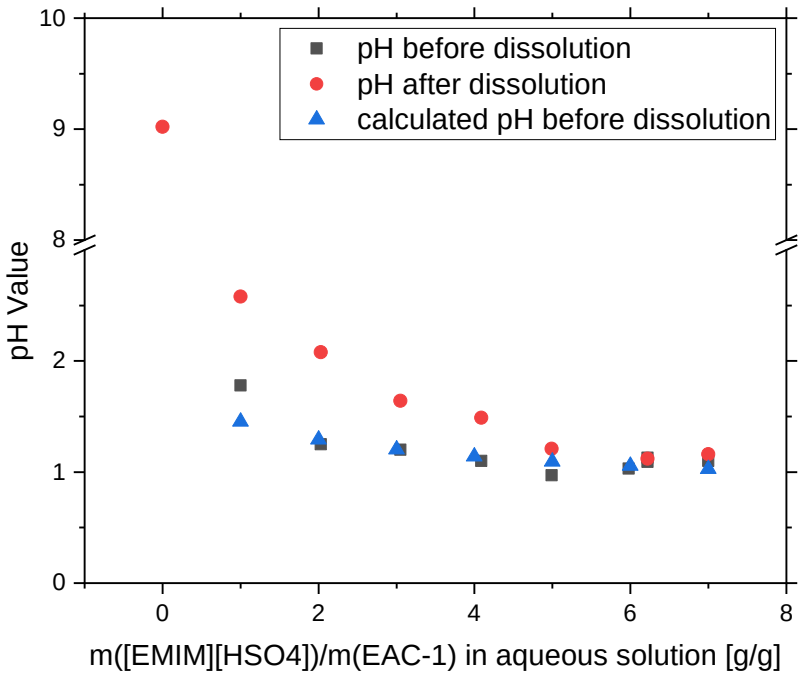

Figure 14: Graph showing the measured and calculated pH dependence of the aqueous [EMIm][HSO$_4$] solution in relation to the ionic liquid amount per one gram of EAC-1.

Comparing the calculated pH values with the measured pH values before dissolution, one can see that they match very well. Only if just one gram of IL is added to the solution, the measured pH is significantly higher than the calculated pH. Additionally, if no IL is added at all to the suspension a pH of 9.02 is measured. This is in accordance of the previous observation that several EAC-1 components react with water alone. This means that the pH increase most likely comes from the reaction of CaO with H_2O (Equation 5), since CaO is the most abundant of all the water soluble fractions. It is also evident that the pH-value increases significantly after the dissolution step. This means that protons must be consumed to dissolve regolith, which supports the postulated dissolution mechanism (Equation 1) of metal oxides in this acidic aqueous ionic liquid mixture. Interestingly the pH-value appears not to change significantly anymore as soon as an excess of 6 g IL is used per gram of EAC-1. This coincides with the observation that increasing the excess of IL beyond 6 g per g of regolith does not further increase dissolution.

3.1.3 ICP-OES

The EAC-1 solutions were analyzed by ICP-OES. As described in Section 2.8, samples were taken from the aqueous solution directly after the vacuum filtration step. Thus the ICP-OES measurement delivered the metal ion concentration in those samples and the mass of each dissolved metal in the aqueous solution $m_{\text{metal ion in solution}}$ after the dissolution step could be calculated. This was achieved by multiplying the metal ion concentration as obtained by the ICP-OES measurement $c_{\text{ICP-OES}}$ with the total amount of aqueous solution V_{total} after the filtration step, as shown in Equation 14.

$$c_{\text{ICP-OES}} \cdot V_{\text{total}} = m_{\text{metal ion in solution}} \tag{14}$$

Since regolith residue was washed with de-ionized water during filtration, the amount of aqueous solution differed for each sample and is listed in Table 5. The error introduced from this washing step could be an explanation for the unsteady dissolution correlation as seen in Figure 15.

Table 5: Volume of aqueous liquid after filtration

m([EMIm][HSO$_4$])/m(EAC-1) [g/g]	0	1	2	3	4	5	6
V_{total} [ml]	46.5	41	29.5	35	27	30	15

Using this information, the mass of each metal ion in solution was calculated and the column chart in Figure 15 was constructed.

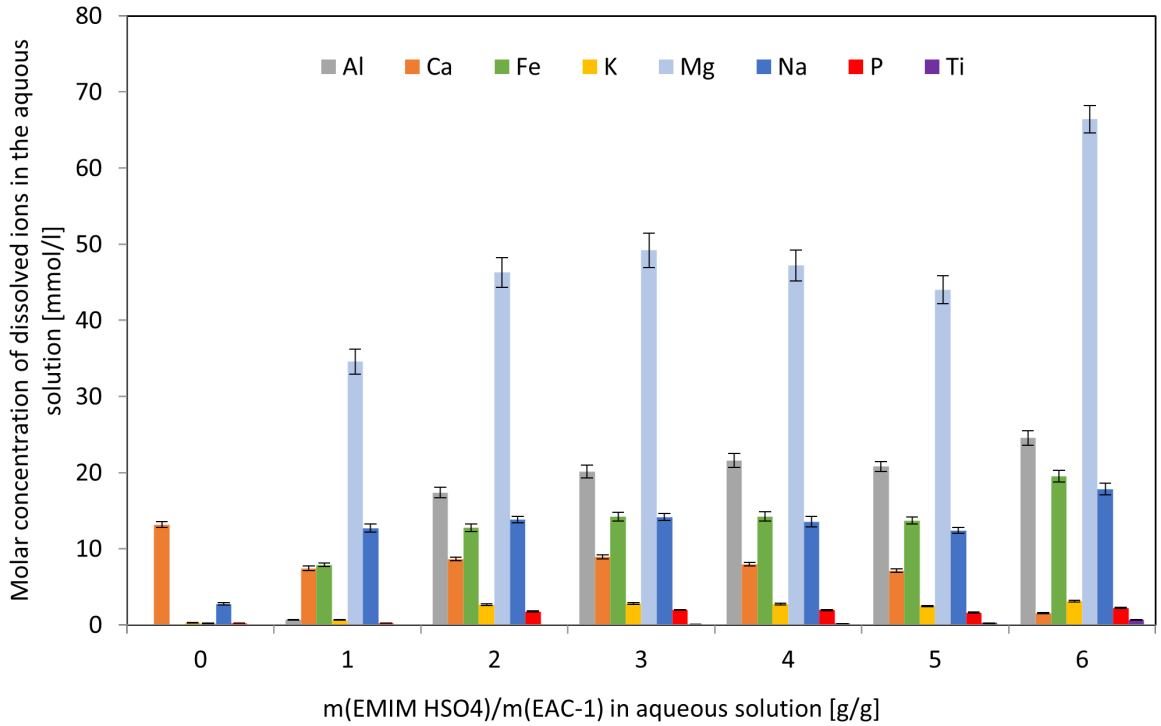

Figure 15: Column chart showing the molar concentration of dissolved metal species in the aqueous solution depending on the [EMIm][HSO$_4$] concentration.

The ICP-OES data shows that without adding any IL, only the water soluble sodium and calcium oxide fractions dissolve. If 1 gram or more of the IL is added, a variety of different ions like Fe, Mg, and Al are observable in the solution. It is interesting to note that the total amount of dissolved material increases if IL is added to the mixture, but it does not seem to make a big difference if two or five grams of IL ares used. Yet if six grams of IL are added per one gram of EAC-1, a jump in the total amount of dissolved metal species is observed, as it has also been discussed in Sections 3.1.1 and 3.1.2.
To get a better understanding of the relative percentage of dissolved oxides, another diagram was constructed relating the amount of dissolved metal species to the respective fraction of oxides in the EAC-1 regolith simulant (Table 1). It needs to be pointed out, however, that the fractions of metal oxides in EAC-1 were determined via EDX, and thus are only semi-quantitative.

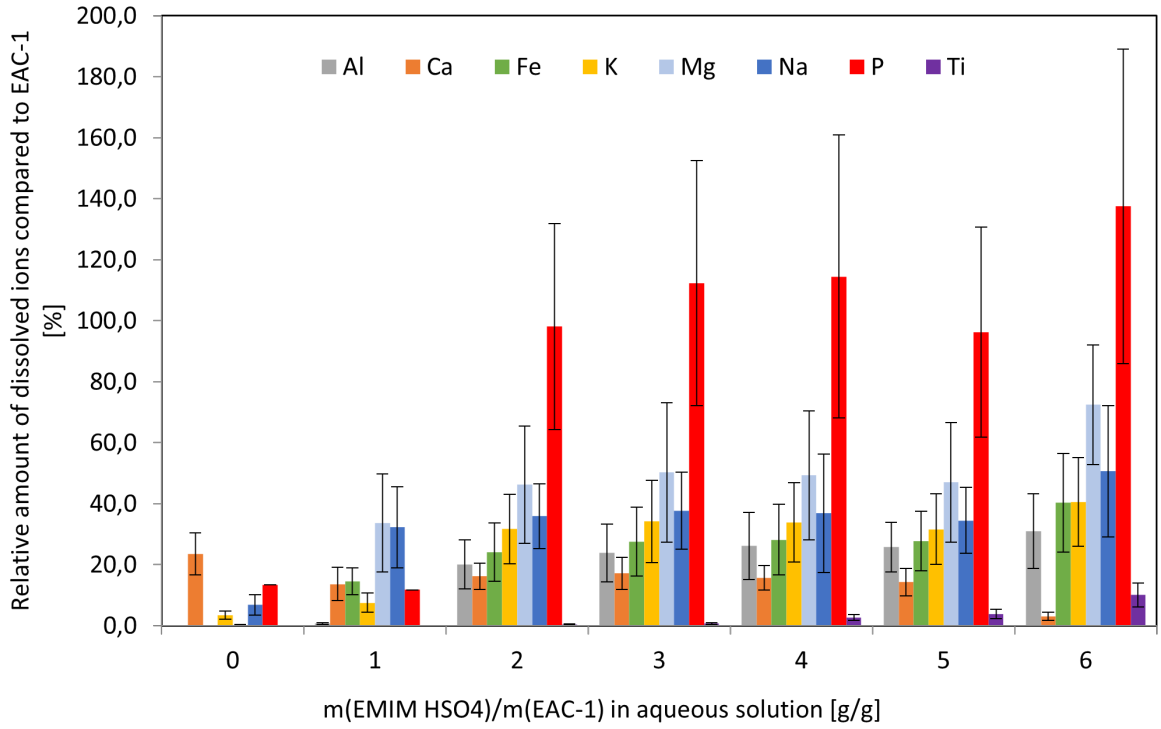

Figure 16: Column chart showing the relative amount of dissolved oxides in the aqueous [EMIm][HSO$_4$] solution.

From the column chart in Figure 16 it becomes apparent that if 2 grams or more of IL are used, all of the phosphorous oxide is completely dissolving. Several of the data-points from phosphorus oxide are above 100 % and thus unrealistically high, yet 100 % is always within the error margins. These high values could also be a result of the imprecise EDX analysis of EAC-1. If 6 grams of the IL are used, up to 72±20 % of the magnesium oxide dissolve, which is the best dissolving oxide except phosphorus oxide. Note that at the highest IL concentration up to 10±4 % of titanium oxide are dissolving. Interestingly, contrary to all other ions the amount of dissolved calcium is decreasing the more IL is added. The cause for this might be that calcium is reacting with HSO_4^- and water to form calcium sulfate dihydrate (gypsum), which has a low solubility [27].
By summing up the mass of all metal ions at each step, a total dissolution percentage was obtained. With this method, Figure 17 was created, in which the dissolution percentages determined from the gravimetric data and from ICP-OES data are shown.

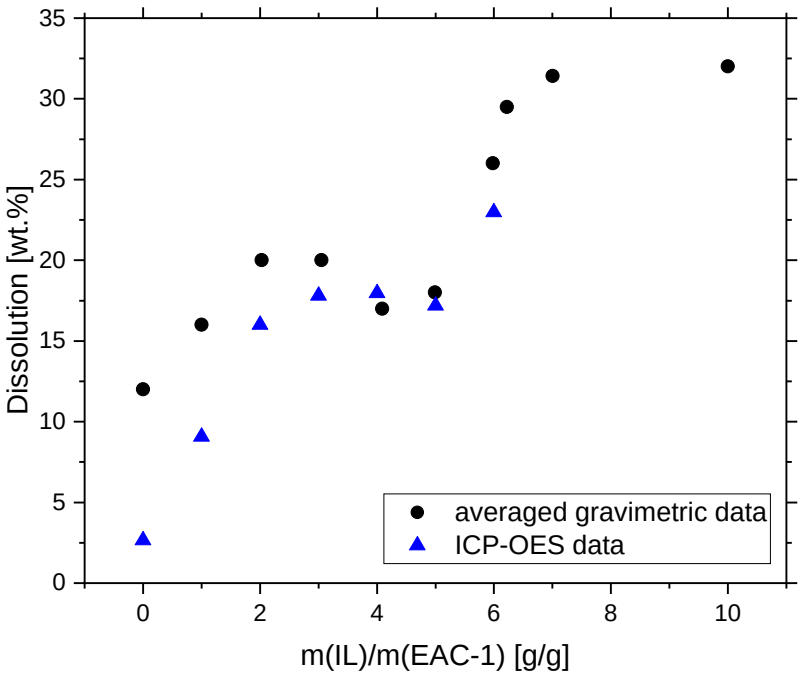

Figure 17: Dissolved fraction of EAC-1 obtained from gravimetric data and from metal ion concentrations measured with ICP-OES.

In Figure 17 it can be seen that the correlation between the ICP-OES and the gravimetric data is getting better the higher the amount of added IL is. A reason for this might be an observed precipitation in the filtrate. This precipitated formed after the filtration step and the amount of precipitate increased at lower IL concentrations. It seems that the increased amount of IL, which also significantly lowers the pH value, stabilizes ions in the solution even after the dissolution step. Thus a high acid concentration with a pH of 2 or lower might be necessary to keep ions in solution, even after the dissolution step.
Since both curves converge at higher IL concentrations, all dissolved metal species must have been detected and included in the calculation, verifying the ICP-OES measurement. It would be beneficial to conduct more ICP-OES measurements at mass ratios of 7 m(IL)/m(EAC-1) and higher, yet the fundamental qualitative information of which metals are in solution and at which concentrations, can already be answered with this data.

3.2 Regeneration of the ionic liquid

As shown in the previous sections, several fractions of the EAC-1 simulant can be dissolved and water is formed. To reuse the IL, dissolved metals have to be removed by electrochemical deposition from the solution at the cathode (electroplating), while simultaneously restoring acidity by oxidizing hydrogen at the anode. This section focuses on investigating this challenge by characterizing the IL with electrochemical methods and electron microscopy. Two sources claim that anodic hydrogen oxidation is possible in protic ionic liquids [28, 29], thus this work prioritizes the investigation of cathodic metal ion reduction.

3.2.1 Electrochemical potential window of [EMIm][HSO_4]

The electrochemical potential window describes the potential range in which a substance is neither oxidized nor reduced. This is of high importance for the electrolyte, since it must remain stable while experiments are carried out. It can be calculated by subtracting the reduction potential from the oxidation potential. In this work, the potential window was investigated with cyclic voltammetry, using different electrode materials and incrementally changing the vertex potentials until reduction and oxidation reactions were evident. A cut-off current density of ± 1 mA/cm^2 was chosen to determine the limiting potentials, as it is a common value used in the literature [30].
All following cyclic voltammograms have the respective start potentials (SP) noted in the legend of the corresponding figure. The starting potentials were always chosen to be at the open circuit potential of the solution. Additionally, the sweep direction is indicated with arrows in the cyclic voltammograms.

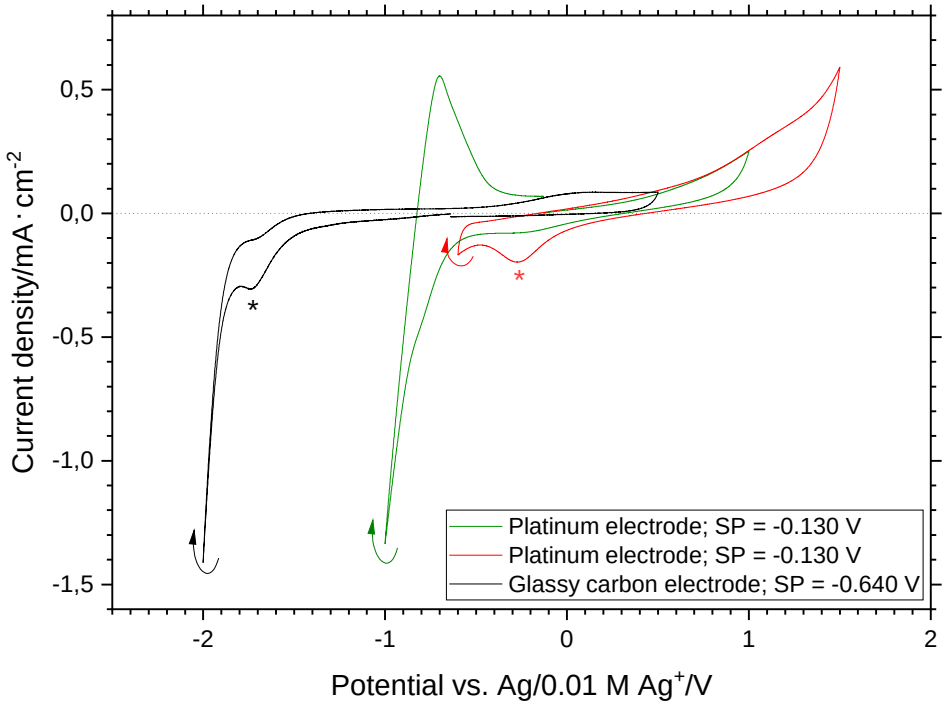

Figure 18: Cyclic voltammograms recorded in [EMIm][HSO_4] with a sweep rate of 100 mV/s, at 70 °C with 3 mm diameter disk electrodes of different materials.

The cyclic voltammograms recorded with a platinum electrode in Figure 18 indicate that at a potential of above about +1 V vs Ag/Ag^+ an oxidation reaction occurs. If a cyclic voltammogram is recorded with an upper vertex potential of +1.5 V (red curve), a new cathodic peak appears, which is marked with a red asterisk. This peak does not appear if the upper vertex potential is at or lower than +1 V, thus it must be the reduction peak of some oxidized component of the ionic liquid. In the cyclic voltammogram of platinum with a cathodic switching potential of -1 V (green curve) a strong reduction current is observed towards the cathodic switching potential, followed by a pronounced anodic peak. This appears to be the reduction of HSO_4^- from the Brønsted acidic ionic liquid to hydrogen as described in Equation 15, followed by the subsequent oxidation of hydrogen which is adsorbed to the poly-crystalline platinum surface. According to Trasatti and Petrii [31] a charge of 210 µC is consumed for the adsorption of a 1 cm^2 monolayer hydrogen on poly-crystalline platinum. Thus a 3 mm diameter disk electrode requires 15 µC to be fully covered in a monolayer of adsorbed hydrogen. An analysis of the anodic peak of the green curve in Figure 18 with NOVA 1.11 revealed it has a charge of 12 µC. Assuming minimal surface roughness leads to the conclusion that about 80 % of the platinum surface

was covered with adsorbed hydrogen.

$$2\,HSO_4^- + 2\,e^- \longleftrightarrow H_2 + SO_4^{2-} \tag{15}$$

This cathodic reaction limits the potential window. In an attempt to increase the hydrogen evolution over potential, the electrode material was changed from platinum to glassy carbon. As it ca be seen in the black curve in Figure 18, this lead to a drastic increase of the cathodic potential limit from -0.6 V to about -1.5 V. One can also see that a new peak appears as marked with a black asterisk, before the pronounced reduction reaction (most likely hydrogen evolution following Equation 15 as discussed previously) starts.
Additionally, the effect of water on the potential window was looked into, since water has a thermodynamic potential window of only 1.23 V. The certificate of analysis of [EMIm][HSO_4] (Figure A2) shows that the chemical has a water content of less than 0.5 wt.%. To investigate whether this water content affects the electrochemical potential window, the ionic liquid was dried under vacuum according to Section 2.3.

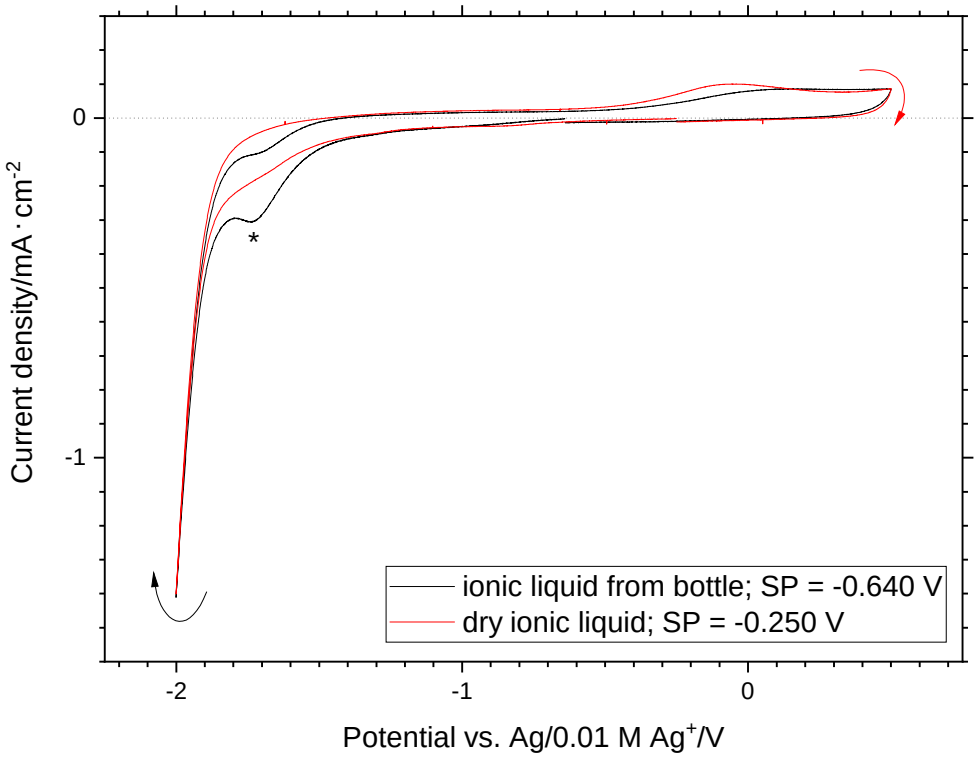

Figure 19: Cyclic voltammograms recorded with a sweep rate of 100 mV/s, at 70 °C in [EMIm][HSO_4] with a 3 mm diameter glassy carbon disc electrode.

The effect of drying the ionic liquid can be seen in Figure 19. As determined via a Karl-Fischer titration, the ionic liquid from the bottle had a water content of 0.22 wt.% and

the dried IL had a water content below the detection limit of the device. According to the device manual, the detection limit in liquid systems is 5 ppm. The black curve, representing ionic liquid directly from the bottle, shows a non reversible reduction peak at about -1.73 V, as indicated by the black asterisk. The red curve on the other hand, which was recorded in the dried ionic liquid, does not show a distinct peak at this position. Hence, this cathodic peak is originating from a reaction of water, like the reduction of oxonium ions formed through the protolysis of bisulfate with residual water, and not form the reduction of the ionic liquid according to Equation 15. Yet, compared to less negative potentials, there still is an increased current flowing at -1.73 V in the red curve. This means that some residual water is still present the dried ionic liquid mixture. However, since the drying step had a pronounced effect and somewhat increased the potential window, it was implemented before all of the following measurements.
In conclusion, [EMIm][HSO_4] shows good electrochemical stability, yet the cathodic potential limit strongly dependents on the electrode material and water content. An anodic potential limit of about >1 V vs. Ag/Ag^+ was determined. The anodic potential limit was not studied in great detail, since hydrogen oxidation in protic ionic liquids has already been demonstrated [28, 29] and this work focused on the cathodic potential limit due to the importance of depositing metals from the EAC-1 solution. The cathodic potential limit is determined by the hydrogen evolution reaction which starts at -1.95 V in a dried ionic liquid at a glassy carbon working electrode. Thus [EMIm][HSO_4] has an electrochemical potential window of at least 2.95 V.

3.2.2 Cyclic voltammetry of EAC-1 dissolved in [EMIm][HSO_4]

Figure 20 shows the cyclic voltammogram of dissolved EAC-1 regolith simulant and of the pure dried ionic liquid. The open circuit potential (OCP) of the EAC-1 mixture was -0.380 V. The blue line representing the EAC-1 solution exhibits a prominent pair of peaks with the cathodic peak 'a' at a potential E_p^{red} of -598 mV with a peak current density j_p^{red} of -0.367 mA/cm^2 and the anodic peak 'b' at a potential E_p^{ox} of -331 mV with a peak current density j_p^{ox} of 0.338 mA/cm^2. In cyclic voltammetry peak pairs are typical for a reversible or quasi-reversible electron transfer reactions. In the ideal case the peak potential separation ΔE_p for an electrochemically reversible system should be 59/n mV (n is the number of electrons, which are transferred) at 25°C and the ratio of the reverse over the forward peak current should be 1 [32]. In this curve however, the peak potential separation ΔE_p is 267 mV and thus much bigger than the theoretical value of 59 mV for one-electron transfer reactions. Also the ratio of peak current densities with $j_p^{ox}/j_p^{red} = 0.92$ is not at the theoretical value of 1 for an electrochemically reversible

system. Thus this reaction is most likely quasi reversible and rate limited by the kinetics of the electron transfer step. By varying the scan rate, this behavior could be further investigated, yet this was not of critical importance to the scope of this project.

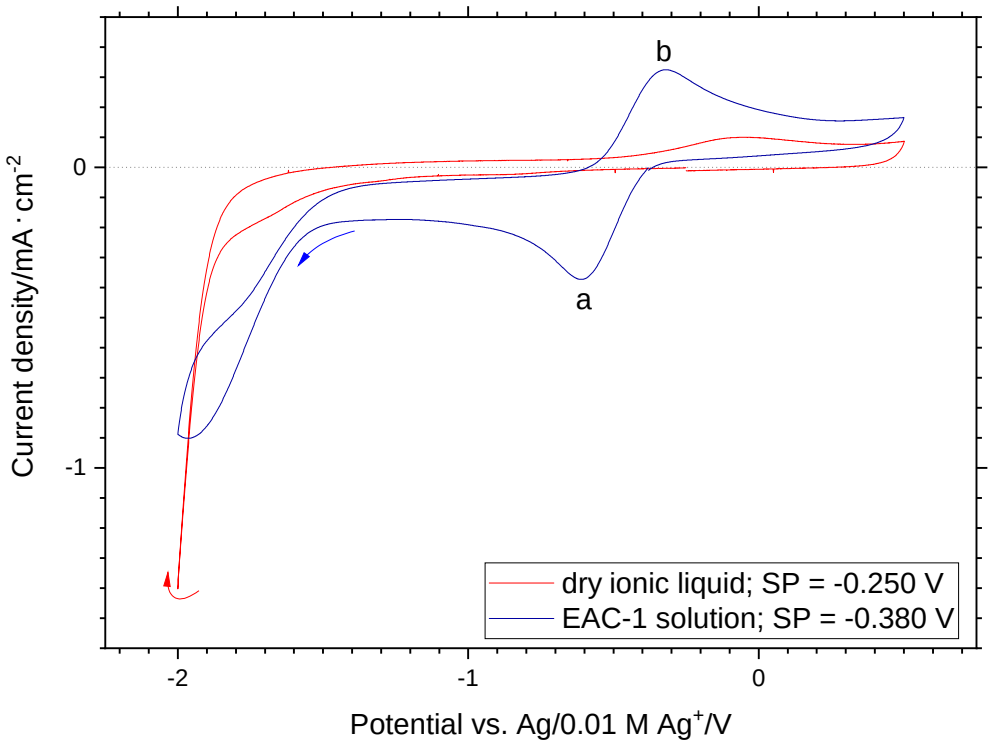

Figure 20: Cyclic voltammograms of dissolved EAC-1 and dried ionic liquid recorded with a sweep rate of 100 mV/s, at 70 °C with a 3 mm diameter glassy carbon disc electrode.

However, the type of electroactive species causing this reaction was of high importance to this project, in order to regenerate the IL via electrodeposition of metals. The only dissolved metal which can exhibit this quasi reversible behavior of freely diffusing species is iron, since it has two stable oxidation states (Fe^{2+} and Fe^{3+}) which can remain in solution. Also the standard electrode potentials of metal species present in the EAC-1 solution (Table 6) indicate that the peak pair is almost certainly caused by the iron redox couple, since all other present metal ions have far more negative standard potentials. Note that the standard electrode potentials were determined in an aqueous solution and can only be used as rough reference points for experiments conducted in different solvents like [EMIm][HSO_4]. Snook et al. [33] state that in broad terms the Ag/Ag^+ electrode has a potential similar to the standard potential of Ag^+ (+0.799 V vs. SHE). Using this information all standard potentials in Table 6 were transformed to V vs. Ag/Ag^+ values. Note that in that paper a different IL (1-butyl-1-methyl-pyrrolidinium

Table 6: Standard electrode potentials of substances found in EAC-1 in aqueous solution at 25°C in V vs. SHE [32] and transformed to V vs. Ag/Ag^+ [33].

Reaction	**Potential vs. SHE [V]**	**Potential vs. Ag/Ag^+ [V]**
$K^+ + e^- \longleftrightarrow K$	-2.925	-3.724
$Ca^{2+} + 2\,e^- \longleftrightarrow Ca$	-2.84	-3.639
$Na^+ + e^- \longleftrightarrow Na$	-2.714	-3.513
$Mg^{2+} + 2\,e^- \longleftrightarrow Mg$	-2.356	-3.155
$Al^{3+} + 3\,e^- \longleftrightarrow Al$	-1.676	-2.475
$2\,H_2O + 2\,e^- \longleftrightarrow H_2 + 2\,OH^-$	-0.828	-1.627
$Fe^{2+} + 2\,e^- \longleftrightarrow Fe$	-0.44	-1.239
$H^+ + e^- \longleftrightarrow H_2$	0.0000	-0.799
$Fe^{3+} + 3\,e^- \longleftrightarrow Fe^{2+}$	0.77	-0.029

bis(trifluoromethanesulfonyl)imid) and a different silver salt (silver trifluoromethane sulfonate) were employed, making this a rough approximation since changing silver salts or ionic liquids could alter the reference potential by up to 760 mV [21].
Nonetheless, since the standard electrode potential is obtained from thermodynamic equilibrium conditions, the order of reaction potentials should remain mainly unaffected by the chosen electrolyte (and also the type of reference electrode). Thus the main takeaway message from Table 6 is that after H^+ ions, iron is the most likely ion in the EAC-1 solution to be reduced and oxidized.
Additionally to the peak pair, a more pronounced reduction is evident in the EAC-1 solution at the cathodic end of the potential window. This reduction seems to be irreversible, since no anodic peak is observed in the reverse scan. It might be the reduction of oxonium ions formed through bisulfate dissociation with residual water in the solution, because it is in the range of -1.73 V, where a similar reduction occurs in the black curve of Figure 19. Unfortunately, a water determination by Karl-Fischer titration was not possible since the solution was too viscous and did not dissolve readily in the Karl-Fischer solvent, leading to unreliable results. It is also possible that the reductive currents in this region might originate from the deposition of dissolved metal ions according to Equation 16.

$$M^{n+} + ne^- \longrightarrow M \tag{16}$$

Finally one can see at the very left end of the cyclic voltammograms, that the EAC-1 soltuion has a lower current density than the dry ionic liquid solution. One possible explanation for this is that the EAC-1 solution has a decreased hydrogen sulfate activity since it was consumed according to Equation 1 during regolith dissolution. This decreases

the hydrogen evolution side reaction (Equation 15). Another reason could be that residual water is reduced to OH^- ions as shown in Table 6, which react with metal ions to form metal hydroxides precipitating on and thereby passivating the electrode. This could be one explanation for the quasi-reversible behavior of the Fe^{+3}/Fe^{+2} couple.

3.2.3 Potential controlled electrolysis experiments

Several potential controlled electrolysis experiments were conducted at cathodic potentials with the goal of investigating the possibility of metal deposition and regeneration of the ionic liquid. Exchangeable 5 mm diameter carbon disk electrodes were used which can be removed from the electrode assembly as described in Section 2.9, so that they could be mounted onto an electron microscope sample holder. Unfortunately, only one exchangeable glassy carbon electrode was available while the others were made of graphite composite. Thus the results of the graphite composite electrodes are not fully comparable to those obtained with glassy carbon, yet the experiments were carried out to gain a proof of concept and investigate if metal deposition from [EMIm][HSO_4] under these conditions is possible.

These preparative experiments were carried out under constant hydrogen gas purging and stirring with a magnetic stir bar, to ensure high convection in the solution. Hydrogen was used instead of an inert gas, to depolarize the anode and to regenerate the bisulfate ions consumed during dissolution of the EAC-1 according to Equation 3.

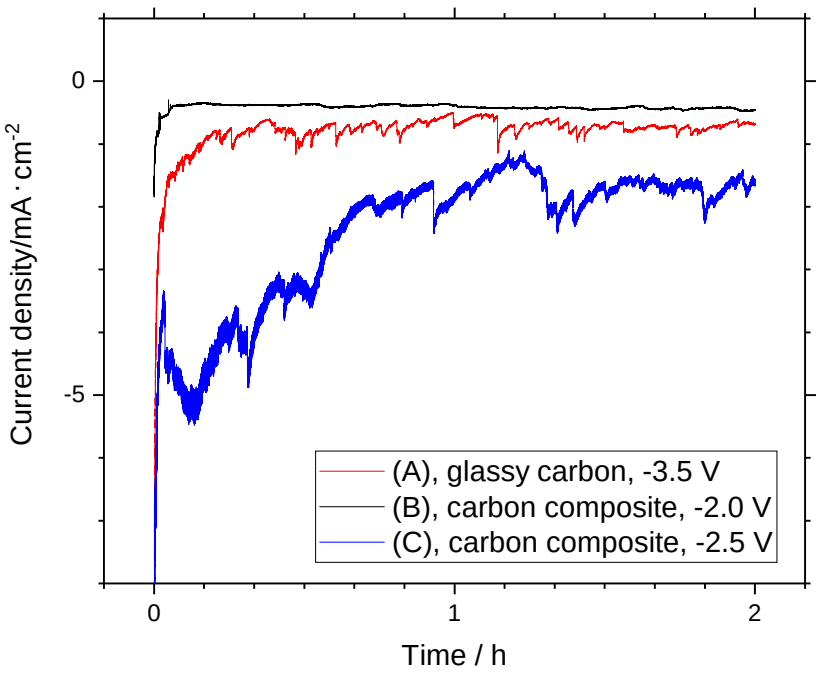

Figure 21: Current-time curves of three potential-controlled electrolyses of EAC-1 dissolved in [EMIm][HSO_4] at three different potentials. The sample names, electrode materials was well as the step potentials are noted in the legend.

All electrolyses were performed at very negative potentials of -2 V, -2.5 V and -3.5 V vs. Ag/Ag^+ to ensure metal ion reduction takes place, even though hydrogen evolution occurs at these potentials, as shown in the previous sections. All electrodes had an OCP of -0.40 V before the electrolysis. In Figure 21 the current-time curves of three different experiments are plotted. Quite unexpectedly, the blue curve of the carbon composite electrode, which was held at a potential of -2.5 V, showed the highest current density of all three experiments. One would expect the current density to increase with increasingly negative potentials, since more reactions are enabled as observed in the cyclic voltammograms of Figure 20. The glassy carbon electrode at -3.5 V (red curve) and the carbon composite electrode at -2.5 V show random current fluctuations, probably caused by the formation of hydrogen gas bubbles which interfere with the mass transport to the electrode surface. The total charge consumed is 0.58 C, 1.14 C and 3.40 C for the carbon composite electrode at -2.0 V (Sample B, black curve), the glassy carbon electrode at -3.5 V (Sample A, red curve) and the carbon composite electrode at -2.5 V (Sample C, blue curve) respectively. Assuming electrodeposition of only iron (three electron transfer, density = 7.874 g/cm^3, molar mass = 55.8450 g/mol) onto the electrode, one obtains a

nominal layer thickness of deposited material of 0.7, 1.4 and 4.2 µm for sample B, A and C respectively.
Upon inspection with the naked eye, the electrode surfaces had not discolored significantly after the experiment. The sample surfaces were characterized with an electron microscope equipped with a secondary electron (SE) detector delivering high depth of field and a back scattered electron (BSE) detector to obtain element contrast. Additionally, the microscope was equipped with an EDX detector, delivering elemental composition information. The goal was to determine, if metal deposition had occurred and which metals had been deposited.

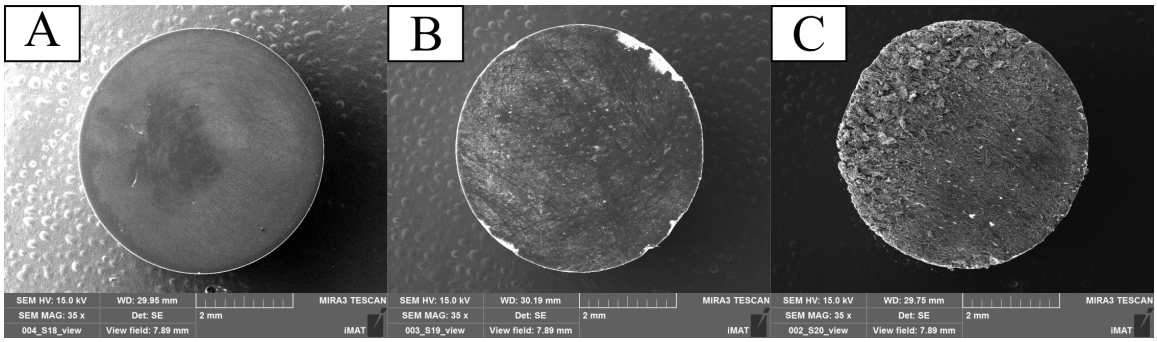

Figure 22: Scanning electron microscope images of three electrodes used in the potential-controlled electrolyses in Figure 21. All images were recorded with a secondary electron detector. The sample name is listed at the top left of each picture.

In Figure 22, it is clear that the glassy carbon electrode (sample A) has the lowest surface roughness of all samples. Sample B and especially sample C have a rough surface, even though they were polished before the experiment. Upon further inspection, it became clear that the carbon composite material of the electrodes B and C was not suitable for the harsh conditions of the potential-controlled electrolyses. Sample B and especially sample C showed significant corrosion and degradation of the surface. This might also explain why the total consumed charge in sample C was higher than in sample A. SEM and EDX investigation did not reveal any significant metal deposition in samples B and C and the resulting pictures can be found in the appendix (Figure A3, A4 and A5).

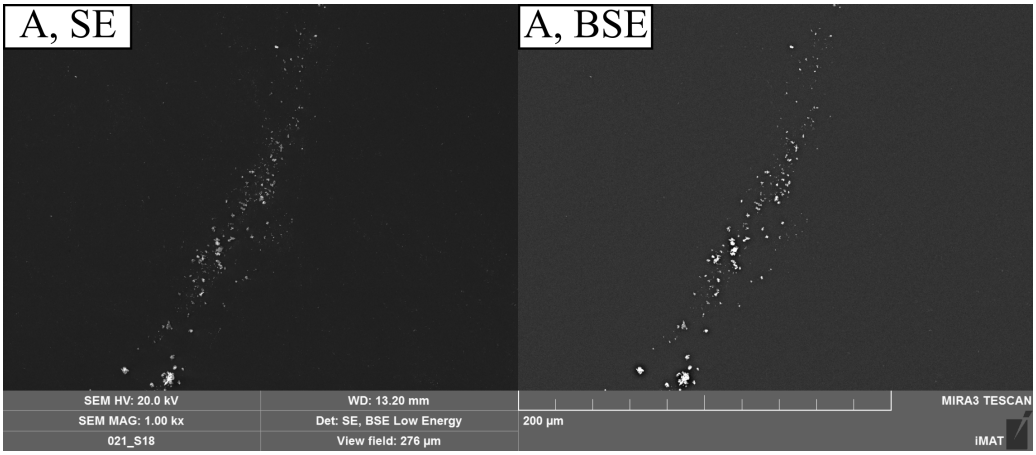

Figure 23: SEM picture of sample A of a region with high contrast recorded with the SE (left) and the BSE detector (right).

In Figure 23, a region with particles showing high contrast on the surface of Sample A is visible. Since the particles also have high contrast with the BSE detector, the elemental composition of the particles must be different from that of the background. Thus it was decided to investigate these particles with EDX.

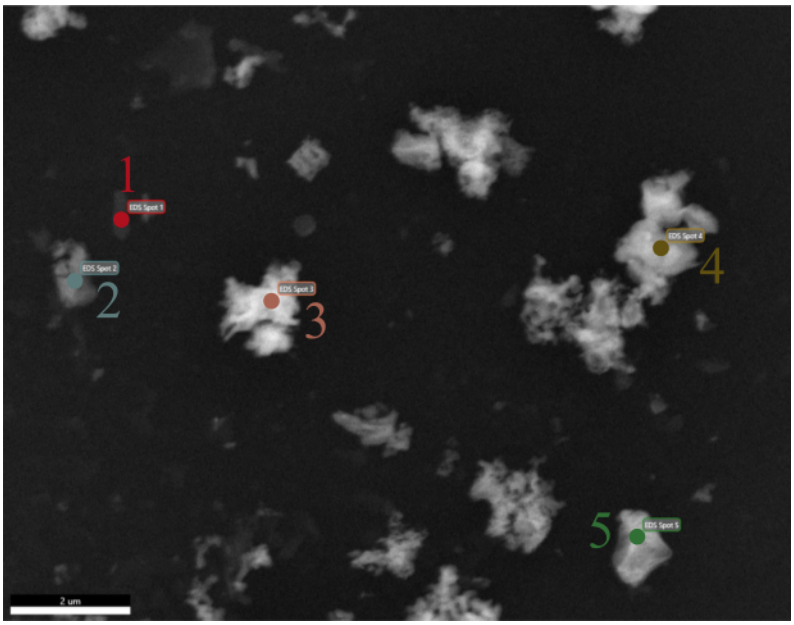

Figure 24: SEM picture highlighting the five EDX measuring spots in the high contrast region of sample A.

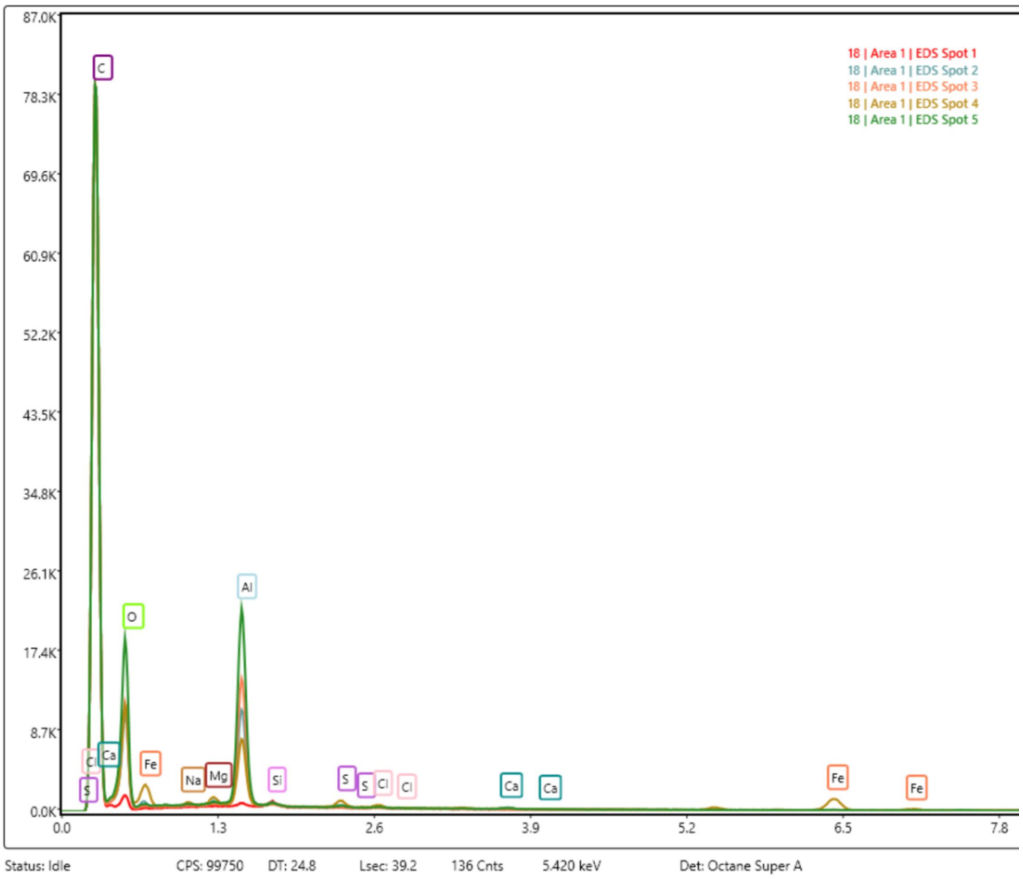

Figure 25: EDX spectra in the high contrast region on the surface of sample A.

From the energy dispersive x-ray spectrum (Figure 25), a quantitative elemental analysis can be conducted at each measuring spot which is shown in Table 7.
The results of this analysis show that even at the spots with high contrast, carbon is the most abundant element followed by oxygen. The elements responsible for the change in contrast seem to be iron and aluminum which were found in small amounts, yet the total metal content appears to be minimal. Additionally, the particles in this high contrast region have a grain size suspiciously similar to that of the aluminum oxide powder used for polishing the electrode. While the polishing powder from Metrohm is listed to have a grain size of 0.3 µm, the particles are smaller than 2 µm and look like agglomerates.

Table 7: Results of the EDX analysis at the high contrast region of sample A at five measuring spots.

Element (Emission line)	**Spot 1** [at. %]	**Spot 2** [at. %]	**Spot 3** [at. %]	**Spot 4** [at. %]	**Spot 5** [at. %]
C (K)	94.40	84.25	83.29	81.66	76.07
O (K)	5.04	13.29	14.08	15.81	20.58
Na (K)	0.09	0.28	0.22	0.37	0.28
Mg (K)	0.08	0.22	0.14	0.30	0.18
Al (K)	0.13	1.74	2.19	1.20	2.75
Si (K)	0.15	0.02	0.01	0.04	0.02
S (K)	0.03	0.08	0.03	0.14	0.05
Cl (K)	0.07	0.04	0.02	0.06	0.03
Ca (K)	0.01	0.06	0.01	0.02	0.03
Fe (K)	0.01	0.01	0.01	0.41	0.01

Thus it is concluded that metal deposition of dissolved EAC-1 in dried [EMIm][HSO_4] using a glassy carbon electrode at a potential of -3.5 V, a temperature of 70 °C, constant hydrogen purging and stirring for two hours was unsuccessful.

3.2.4 Fe(III) addition experiment

In order to verify the assumption that dissolved iron is responsible for the peak pair in Figure 20, the EAC-1 solution was spiked with additional iron ions. Iron(III) sulfate was chosen as an additive, because iron(III) ions were expected to at least partly originate from the magnetic fractions of EAC-1 regolith simulant. The sulfate anion was chosen since it is the deprotonated form of the hydrogen sulfate anion of [EMIm][HSO_4] and thus should not significantly change speciation.

The amount of added iron(III) sulfate was based on the iron concentration determined by the ICP-OES measurement, as discussed in Section 3.1.3. The goal was to roughly double the iron concentration compared to the concentration already present in the EAC-1 solution. As it can be seen in Figure 15, the iron concentration is 19.5±0.8 mM in the aqueous solution where 6 g of IL were used. This would represent an iron concentration of 153 mM in the ionic liquid, if the weight of dissolved metals is ignored and the density is assumed to remain unchanged. Note however, that this value does not directly represent the concentration present in the EAC-1 solution, since this solution was prepared from 28 g of IL per 4 g of EAC-1 (hence 7 g IL per 1 g of regolith). After weight losses from transferring the liquid into the electrochemical cell and from water-content measurements,

the weight of the dry EAC-1 solution was 24.11 g. Assuming all water is removed, the amount of iron ions in that solution should be 2.70 mmol. For this experiment 1.352 g of iron(III) sulfate with a purity of 97 % (Table 2) were weighed in, increasing the total iron concentration 2.2-fold from 153 mM to 339 mM. The substance was dissolved by adding 25 ml of de-ionized water and rigorously stirring the mixture. Finally, the Fe(III)-spiked ionic liquid solution was dried again as described in Section 2.3.

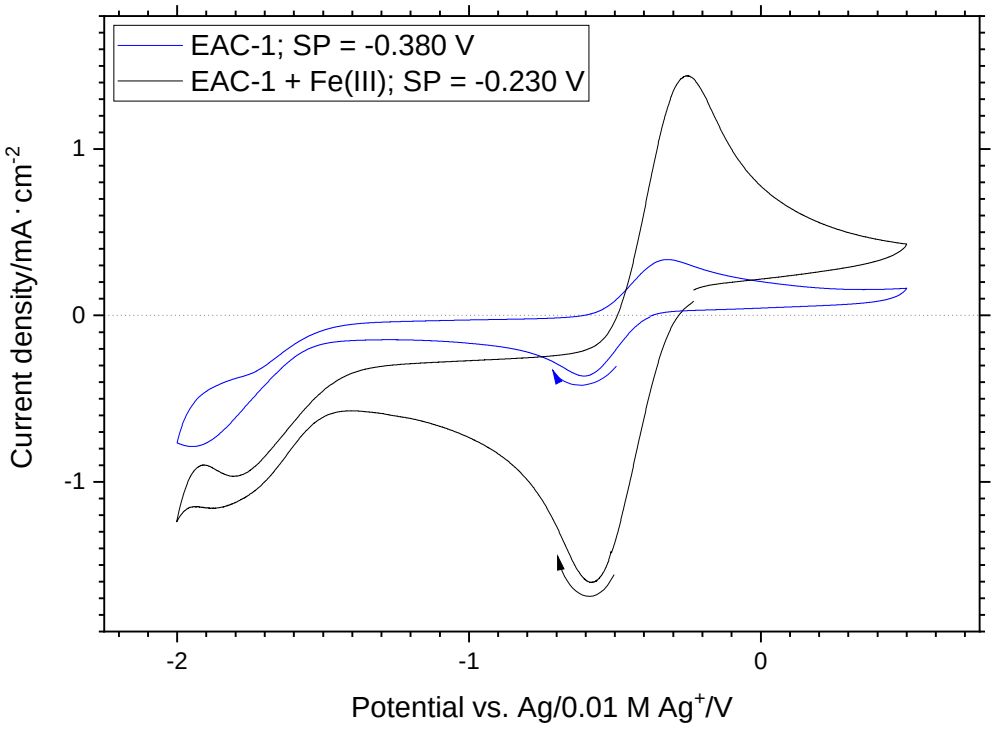

Figure 26: Cyclic voltammograms of the EAC-1 solution and said solution spiked with iron(III) sulfate. The cyclic voltammograms were recorded with a sweep rate of 100 mV/s, at 70 °C with a 3 mm diameter glassy carbon disc electrode.

Table 8: Cyclic voltammetric data and OCP value of the measurements in Figure 26

	E_p^{red} [mV]	E_p^{ox} [mV]	j_p^{red} [mA/cm^2]	j_p^{ox} [mA/cm^2]	OCP [mV]	ΔE_p [mV]
EAC-1	-598	-331	-0.367	0.338	-380	267
EAC-1 + Fe(III)	-563	-263	-1.70	1.63	-230	300

By comparing the cyclic voltammograms of Figure 26 one can see that the current density of the peak pair increases drastically upon iron(III) addition. It becomes also clear that the reduction reaction at the cathodic end of the cyclic voltammogram is largely independent

of the iron concentration. Since the general shape of the CVs remains similar and no new peaks appear, the reason for the increase in current density of the pair of peaks must be the additional iron in the solution. This confirms the assumption that the peak pair is due to the redox reaction of the Fe^{2+}/Fe^{3+} couple according to Equations 17 and 18.

$$\text{Cathodic peak: } Fe^{3+} + e^- \longrightarrow Fe^{2+} \tag{17}$$

$$\text{Anodic peak: } Fe^{2+} \longrightarrow Fe^{3+} + e^- \tag{18}$$

It was tried to correlate peak current density j with the increasing iron concentration since j can be calculated with the Randles–Ševčík Equation 19 at 25 °C [32],

$$j = 2.69 \cdot 10^5 n^{3/2} D^{1/2} c v^{1/2} \tag{19}$$

where j is given in $A{\cdot}cm^{-2}$, n is the number of electrons, D is the diffusion coefficient in $cm^2{\cdot}s^{-1}$, c is the concentration of electrochemically active species in $mol{\cdot}ml^{-1}$ and v is the scan rate in $V{\cdot}s^{-1}$. According to this equation, the current density is directly proportional to the concentration of electro-active species, which is dissolved iron in this case. Thus a 2.2-fold increase of j is expected, if D is concentration independent, yet the value increased 4.6-fold from -0.367 to $-1.70\ mA/cm^2$ in the reductive peak. Likely explanations for this deviation are that D is most certainly concentration dependent and therefore different in both solutions. In addition, this method of concentration determination is only suitable if exclusively one species of iron is present. Yet one can already see in the EAC-1 curve that the OCP lies in-between E_p^{red} and E_p^{ox}, while the OCP of the spiked EAC-1 curve is even higher than the respective E_p^{ox}. This behavior hints that there must be a substantial amount of Fe^{2+} in the EAC-1 solution already and thus a concentration determination of the total iron content via the Fe^{3+} reduction peak cannot be accurate.
Furthermore it was tried to correlate the iron concentration change with shifts of the OCP and the formal potential. The OCP is a result of the Nernst Equation 20 [32]

$$OCP = E = E^{0'} + \frac{RT}{nF} ln \frac{c(Ox)}{c(Red)} \tag{20}$$

where $E^{0'}$ is the formal potential in V, R is the ideal gas constant in $J{\cdot}mol^{-1}{\cdot}K^{-1}$, F is the Faraday constant in $C{\cdot}mol^{-1}$, n is the number of electrons transferred and c is the molar concentration of either the oxidized or reduced species. The formal potential is a useful quantity to circumvent activities which are rarely ever known. It is the measured potential of the half-cell vs. SHE where the oxidized and reduced species are present at

equal concentrations, such that the ratio $\frac{c(Ox)}{c(Red)}$ becomes one. Thus the formal potential contains the standard potential E^0 and the dimensionless activity coefficients γ as seen in Equation 21.

$$E^{0\prime} = E^0 + \frac{RT}{nF} ln \frac{\gamma_{Ox}}{\gamma_{Red}} \tag{21}$$

Considering the reaction of the Fe^{3+}/Fe^{2+} couple, the formal potential $E^{0\prime}$ can be estimated by averaging the voltage of the anodic and cathodic peak potential. This potential is mainly influenced by the overall iron concentration and independent of the oxidation states. In the EAC-1 solution $E^{0\prime}$ is -465 mV and in the EAC-1+Fe(III) solution $E^{0\prime}$ is -413 mV representing a shift of the formal potential by 52 mV. According to the Nernst equation this shift of the formal potential indicates a 7.6-fold increase of the iron concentration. Note however, that there is a large uncertainty introduced since ΔE_p is much bigger than the anticipated 59 mV (the peak potential difference is 267 mV for the EAC-1 solution and 300 mV for the spiked solution).

The OCP on the other hand is depending mainly on the ratio of $\frac{c(Fe^{3+})}{c(Fe^{2+})}$ which is affirmed by its proximity to the formal potential. In relation to $E^{0\prime}$, the OCP is shifted by 85 mV in the EAC-1 solution and by 183 mV in the EAC-1+Fe(III) solution. By again applying the Nernst equation, this shift represents a concentration ratio $\frac{c(Fe^{3+})}{c(Fe^{2+})}$ of 27 and 1264 in both solutions respectively. That concentration increase of the Fe(III) species differs significantly from the experimental expectations (Fe(III) concentration should be roughly doubled) and from the observations made in previous calculations. It might be that the determination of the formal potential is inaccurate not only because of the large ΔE_p, but also due to other components like residual water and dissolved oxygen which might be different in both solutions.

In conclusion, this experiment verified the assumption that the peak pair can be assigned to the Fe^{2+}/Fe^{3+} couple. Another major observation made is that the reductive current at the cathodic end of the cyclic voltammogram appears to be independent of the iron concentration. This means that the reduction occurring in the region of -1.45 to -2 V is not caused by the reduction of Fe(II) to Fe(0).

3.2.5 Characteristics of Fe(III) in [EMIm][HSO_4]

In an attempt to model the EAC-1 solution behavior with an electrolyte of known composition and to reduce the number of experimental variables, a solution containing only iron(III) sulfate in [EMIm][HSO_4] was made. The solution was prepared in a similar way as described in Section 2.2, yet instead of EAC-1 a precise amount of iron(III) sulfate was used to reach a concentration of 0.186 M.

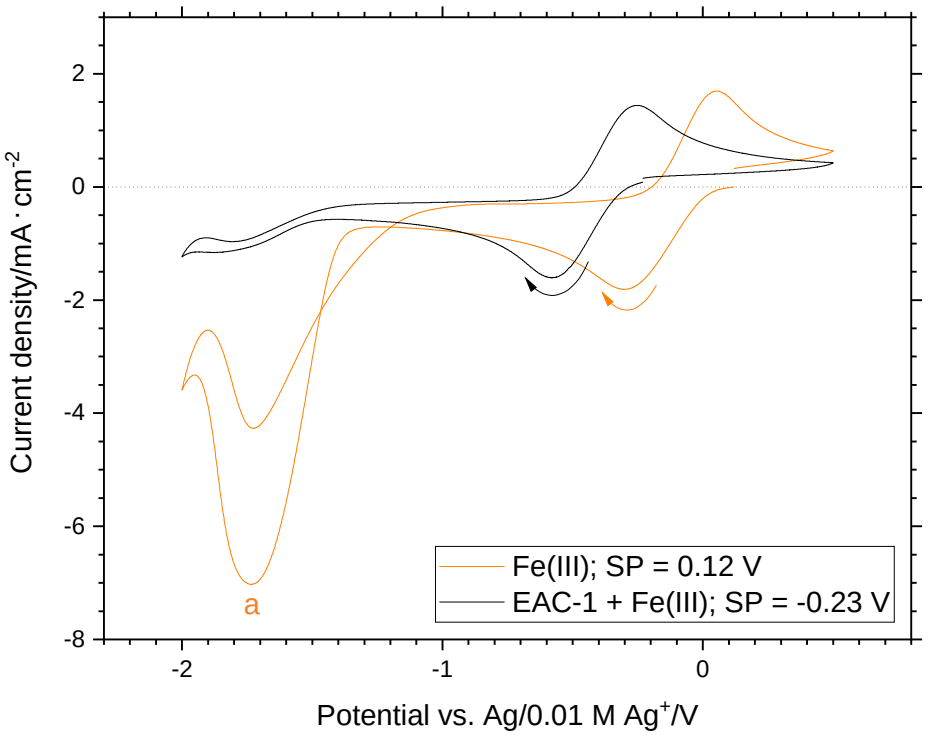

Figure 27: Cyclic voltammograms of the spiked EAC-1 solution and the iron(III) sulfate solution. The cyclic voltammograms were recorded with a sweep rate of 100 mV/s, at 70 °C with a 3 mm diameter glassy carbon disc electrode.

Table 9: Cyclic voltammetric data from Fe(III) solution experiment.

	E_p^{red} [mV]	E_p^{ox} [mV]	j_p^{red} [mA/cm^2]	j_p^{ox} [mA/cm^2]	ΔE_p [mV]
EAC-1 + Fe(III)	-563	-263	-1.70	1.63	300
Fe(III)	-282	41	-1.67	1.77	323

Several interesting observations can be made in the cyclic voltammograms of Figure 27. First there is an apparent shift of the iron redox couple towards more positive potentials. E_p^{red} shifted by 281 mV and E_p^{ox} shifted even more by 304 mV (Table 9). Secondly, a very pronounced reduction is taking place with a peak 'a' at -1.73 V. The peak shape is rather symmetric indicating adsorption. A smaller cathodic peak of similar shape is observed on the anodic return sweep at the same potential.

The potential shift of the Fe^{2+}/Fe^{3+} peak pair can be explained by a change of the iron complex coordination due to the presence of a multitude of different dissolved metal ions in the EAC-1 solution. Another factor responsible for the peak potential and OCP shift

towards more positive values is an increased ratio of Fe^{3+} to Fe^{2+} ions which is discussed in more detail in the previous Section. This means that iron forms a different complex in the solution containing only Fe(III) ions, compared to the spiked EAC-1 solution. The ratio of HSO_4^-/SO_4^{-2} ions in both solutions is also different, since HSO_4^- is consumed to dissolve metal oxides, yet not to dissolve iron(III) sulfate. Thus it seems that iron complex formation is affected either by accompanied dissolved metal ions in the spiked EAC-1 solution or/and by a different HSO_4^-/SO_4^{-2} ratio.

The reduction peak 'a' in Figure 27 might be the reduction of residual water or oxonium ions which also happens at a potential of -1.73 V as shown in Figure 19. Yet it has a vastly increased current density, which is unexpected since both solutions have been dried in a similar manner. Interestingly, this reduction behavior is very inconsistent. Firstly, it was not present in the spiked EAC-1 curve, hinting some property of that solution is suppressing this reduction. Secondly this reduction depends strongly on the open circuit potential at the start of the measurement. The OCP was 0.120 V in equilibrium, yet decreased drastically even below -1 V after CVs or chronoamperometry experiments with vertex or step potentials of -2 V were conducted. The more negative the OCP, the lower the current density of reduction peak 'a'. This whole behavior is demonstrated in Figure 28, where up to 30 cyclic voltammograms were recorded in the Fe(III) solution successively. By setting the lower vertex potential to -2 V the OCP decreased with each scan which affected following scans.

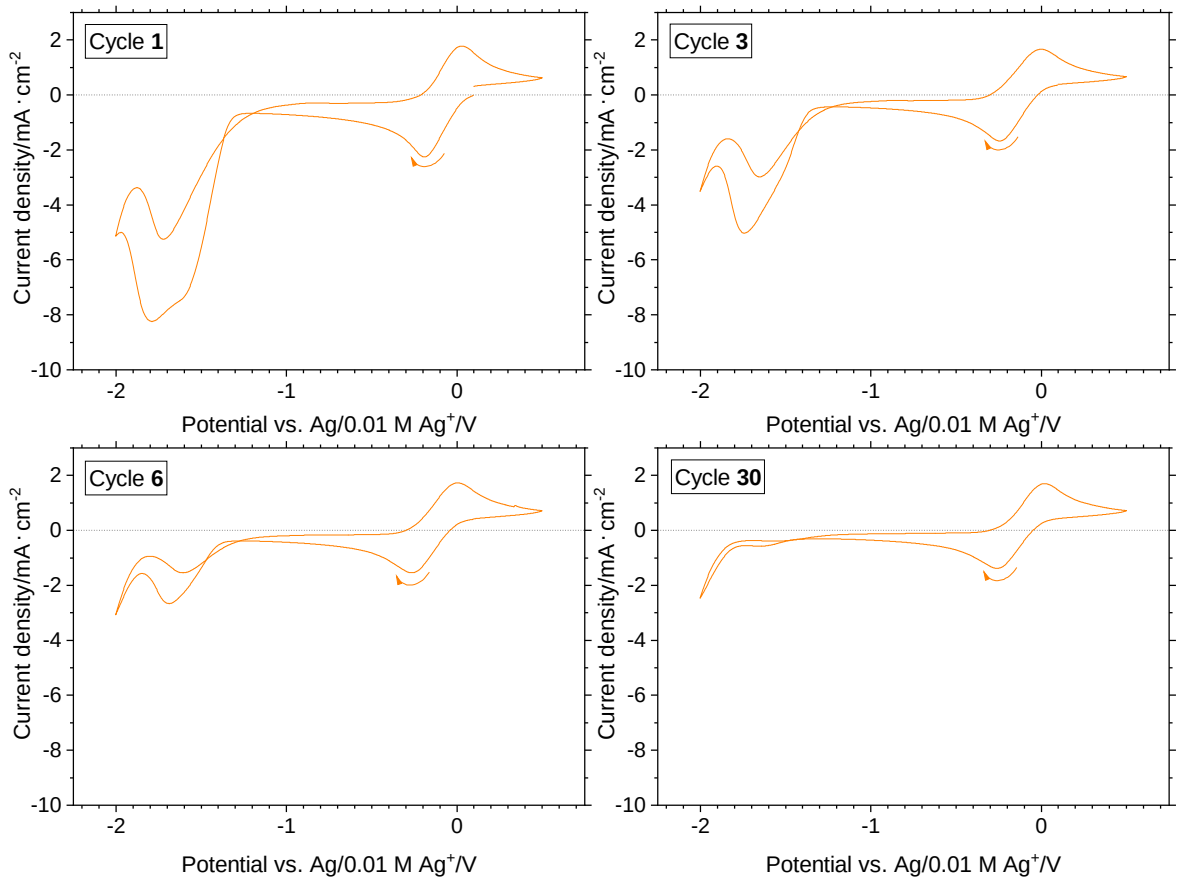

Figure 28: Cyclic voltammograms of the iron(III) sulfate solution. The CVs were recorded in succession during a multi cycle experiment using the same experiment parameters. Up to 30 CVs were recorded and the scan number can be seen in the top left corner of each graph. The cyclic voltammograms were recorded with a sweep rate of 100 mV/s, at 70 °C with a 3 mm diameter glassy carbon disc electrode. The start potential (SP) of the experiment was 0.120 V.

Table 10: Cyclic voltammetric data from successively recorded cycles of the Fe^{2+}/Fe^{3+} peak pair as seen in Figure 28.

	E_p^{red} [mV]	E_p^{ox} [mV]	j_p^{red} [mA/cm^2]	j_p^{ox} [mA/cm^2]	ΔE_p [mV]
Cycle 1	-181	12	-2.32	2.05	193
Cycle 3	-232	-19	-1.87	1.83	212
Cycle 6	-252	-12	-1.86	1.79	269
Cycle 30	-247	5	-1.65	1.76	251

As described previously, the reduction current in the range of about −1.35 to −1.95 V diminishes (Figure 28). The peak current density j in this reduction region decreased by a factor of 30 from 7.95 mA/cm^2 in the first scan to 4.74, 2.37 and 0.26 mA/cm^2 in the third, sixth and thirtieth cycle. Additionally, a new shoulder appears in the reduction region at around -1.60 V, which is also decreasing with each scan. The reason for this newly appearing shoulder resulting in a different peak-shape compared to peak 'a' of the cyclic voltammogram in Figure 27 is not clear, since both solutions were prepared in the same way. Maybe the water content in both solutions is not exactly equal.
The behavior of decreasing current density seen in Figure 28 means that something is blocking the electrode reaction. The Fe^{3+}/Fe^{2+} equilibrium potential could be calculated with the Nernst Equation 20, yet in this case the equilibrium shifts and is affected by the experimental parameters of preceding experiments. Sweeping to negative working electrode potentials leads to a negative shift of the Fe^{3+}/Fe^{2+} equilibrium potential and of the OCP, which "relaxes" back to 0.120 V after the experiments stop. Thus some reaction changes the electrode surface, causing a temporary shift of the Fe^{3+}/Fe^{2+} equilibrium potential and the OCP. This shift only lasts for a few minutes. We suggest that this behavior is caused by the precipitation of metal hydroxides on the electrode surface, leading to a temporary passivation of the electrode. The cathodic reduction of residual water to hydrogen generates OH^- ions as shown in Equation 22, which can be attributed to the large reduction peak at -1.73 V in Figure 27 and 28. That the reduction at -1.73 V might be caused by water is demonstrated in Section 3.2.1.

$$2\,H_2O + 2\,e^- \longleftrightarrow H_2 + 2\,OH^- \tag{22}$$

The formed hydroxide ions locally increase the pH at the electrode surface in a process already described in literature [34]. They subsequently react with iron and potentially other metal ions in the EAC-1 solution to iron hydroxide according to Equation 23. The metal hydroxide precipitates on the electrode, causing the surface to passivate.

$$Fe^{2+} + 2\,OH^- \longrightarrow Fe(OH)_2 \tag{23}$$

This hypothesis is supported by the increasing peak potential difference ΔE of the Fe^{2+}/Fe^{3+} peak pair, acting as an internal probe for electrode passivation. From Table 10 one can obtain that ΔE increased from 193 mV in the first cycle, to 212, 239 and 251 mV in the third, sixth and thirtieth cycle. This increasing deviation from the anticipated ΔE of 59 mV in reversible one electron transfer systems means, that electron transfer at the electrode surface is continuously hindered [35]. Finally, also the current density of the Fe^{2+}/Fe^{3+} peak pair decreased from cycle to cycle additionally to the decreasing current

density of the reduction at -1.73 V, which is another indication for electrode passivation.

3.2.6 Characteristics of Fe(II) in [EMIm][HSO_4]

During the experiment planning phase it was decided to investigate whether comproportionation reactions of the two iron species Fe(0) and Fe(III) are responsible for the absence of the stripping peak in the potential region in which metal deposition would be expected. Thus an experiment using only Fe(II) was designed.
For this experiment a new Fe(II) solution in [EMIm][HSO_4] was prepared. To get comparable data with respect to previously conducted Fe(III) solution experiments, it was tried to achieve a concentration of 0.186 M, yet Fe(II) sulfate turned out to have a very low solubility in the IL. There still were undissolved solid particles remaining in the solution after the dissolution step. Thus, it was assumed that a saturated solution had been produced and the electrochemical experiment was carried out. As a result of the lower concentration, the peak current densities are significantly smaller than in the 0.186 M Fe(III) sulfate solution.

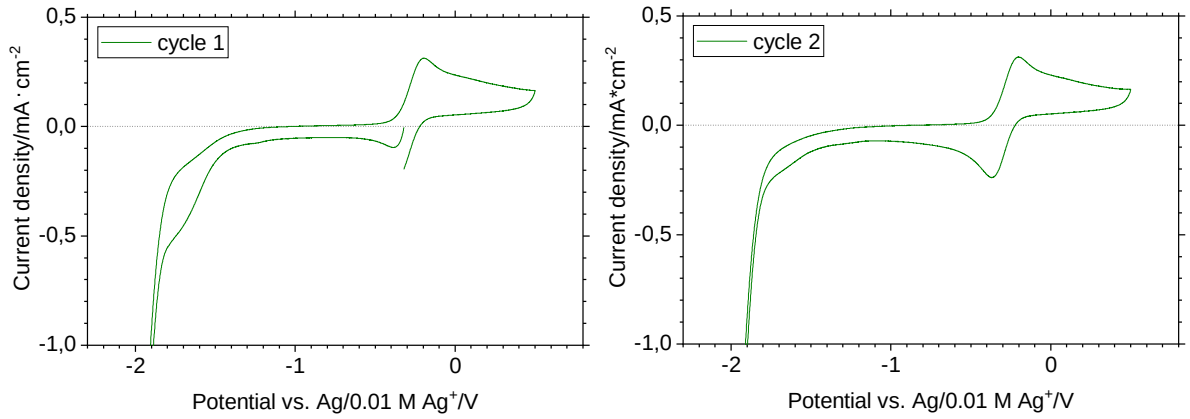

Figure 29: Cyclic voltammograms in the iron(II) sulfate solution. The CVs were recorded in succession during a multi cycle experiment using the same experiment parameters. The cycle number can be seen in the top left corner of each graph. Experiments were carried out with a sweep rate of 100 mV/s, at 70 °C with a 3 mm diameter glassy carbon disc electrode. The start potential (SP) of the experiment, which was equal to the OCP, was -0.320 V.

The high open circuit potential of the Fe(II) solution which lies in-between E_p^{red} and E_p^{ox} indicates that the solution is already partially oxidized by atmospheric oxygen to Fe^{3+}.

Table 11: Cyclic voltammetric data from successively recorded cycles of the iron(II) solution as seen in Figure 29.

	E_p^{red} [mV]	E_p^{ox} [mV]	j_p^{red} [mA/cm²]	j_p^{ox} [mA/cm²]	ΔE_p [mV]
Cycle 1	-380	-208	-	0.302	172
Cycle 2	-360	-216	-0.271	0.302	144

Assuming the diffusion coefficient remains similar for both iron species, one can calculate the Fe(II) concentration since current density is directly related to the concentration of the electrochemically active species as it can be seen in Equation 19 (Randles–Ševčík). Using j_p^{ox} form the first cycle of the Fe(III) and Fe(II) solution (Table 10 and 11) it can be calculated that the current decreased by a factor of 0.15 which would represent an Fe(II) concentration of 0.027 M. The CVs in Figure 29 do not show a distinct Fe(II)/Fe(0) reduction peak, as already expected due to observations made in Section 3.2.4. Instead the peak pair of the Fe(III)/Fe(II) redox couple can be seen again. While there is a small reduction event in the range of -1.50 V to -1.80 V, this is already vanished in the second cycle. These experiments once again confirmed that no iron is deposited in this potential range.

3.2.7 Electrochemical behavior of dissolved Fe(III) in [EMIm][HSO_4] of varying acidity

The peak pair shift of the iron redox couple in the Fe(III) solution with respect to the spiked EAC-1 solution observed in Figure 27 raised several questions and might be explained by the speciation of the iron in the IL. Besides a multitude of different metal ions in the spiked EAC-1 solution, also the acid/base ratio c(HSO_4^-)/c(SO_4^{2-}) was smaller. The EAC-1 solution has a decreased hydrogen sulfate ion concentration because they are consumed to dissolve metal oxides producing water and sulfate ions (Equation 1). In contrast, the Fe(III) solution should have the same hydrogen sulfate concentration as the pure IL, since iron(III) sulfate dissolves readily. This change of hydrogen sulfate ion concentration might change the ligand sphere around the iron ions.
Indeed, in literature there are many well known examples describing a pH dependent formal potential shift of the Fe^{3+}/Fe^{2+} redox couple. In an aqueous solution the formal potential of said redox couple changed from 0.70 V vs SHE in a 1 M HCl solution to 0.53 V vs SHE in a 10 M HCl solution (see Table C.2 in [32]). Thus in the following experiment the hydrogen sulfate ion concentration dependence of the peak pair was investigated,

hoping that it might also deliver some clues regarding the potential shifts described in Section 3.2.5.

In this experiment, the Fe(III)-spiked EAC-1 solution discussed in Section 3.2.4 was re-used, which had a total weight of 25.48 g. By adding defined amounts of pure dried IL to the mixture, the solution is diluted and the hydrogen sulfate ion concentration increases. Since the pH value is only defined in aqueous solutions, it could not be measured directly in the ionic liquid solution. Thus 499 mg of the mixture were removed from the glass cell and weighed with a high precision scale into a 25 ml measuring flask. This flask was subsequently filled with de-ionized water to a total volume of 25 ml and the pH-value of that solution was measured.

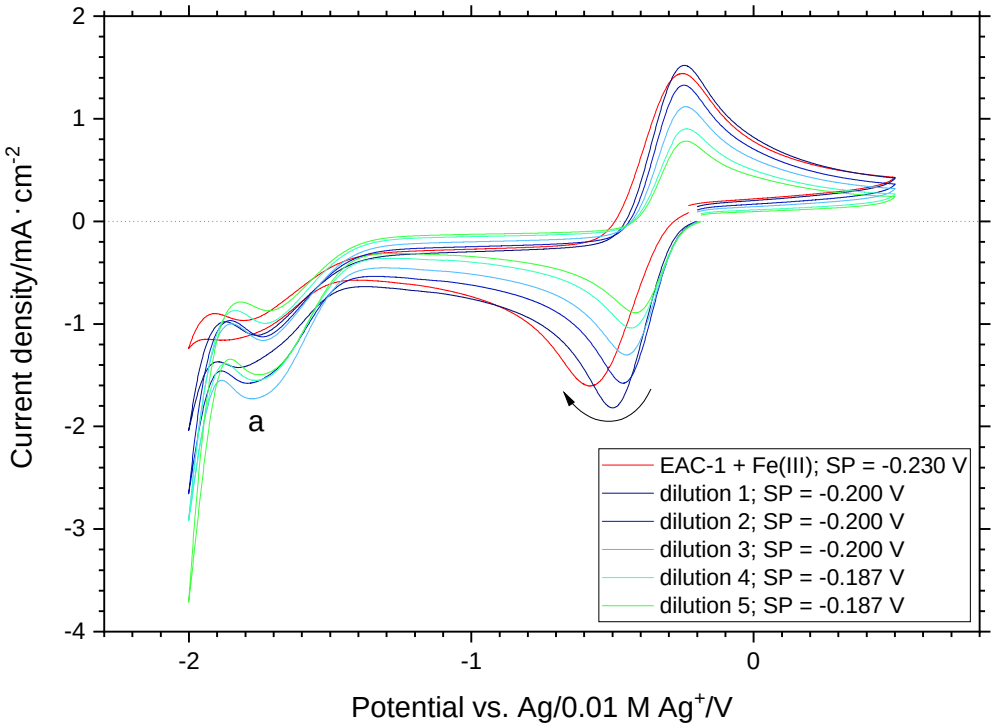

Figure 30: Cyclic voltammograms of Fe(III)-spiked EAC-1 solution (see Section 3.2.4) and of several dilutions of said solution. The cyclic voltammograms were recorded with a sweep rate of 100 mV/s, at 70 °C with a 3 mm diameter glassy carbon disc electrode. The black arrow indicates the sweep direction which remained unchanged for each measurement.

Table 12: Cyclic voltammetric data from Figure 30.

			Fe^{3+}/Fe^{2+}					Peak 'a'	
	Added dry IL [g]	pH-Value*	E_p^{red} [V]	E_p^{ox} [V]	ΔE_p [V]	j_p^{red} [mA/cm^2]	j_p^{ox} [mA/cm^2]	E_p^{red} [V]	j_p^{red} [mA/cm^2]
EAC-1 + Fe(III)	0	1.54	-0.563	-0.263	300	-1.70	1.63	-1.87	-0.72
dilution 1	4.07	1.50	-0.494	-0.256	238	-1.79	1.70	-1.82	-0.88
dilution 2	8.468	1.46	-0.456	-0.255	201	-1.53	1.54	-1.79	-1.14
dilution 3	10.246	1.43	-0.439	-0.246	193	-1.25	1.26	-1.77	-1.42
dilution 4	15.747	1.41	-0.425	-0.245	180	-1.05	1.01	-1.77	-1.25
dilution 5	12.493	1.39	-0.408	-0.249	159	-0.87	0.90	-1.76	-1.27

*pH Value determined by dissolving 499 mg of the solution with de-ionized water in a 25 ml measuring flask

Using the described pH value measuring method, a pH of 1.36 is measured for the aqueous solution of the neat dry ionic liquid. The measured pH values of each solution can be seen in Table 12. A clear trend of the pH value from 1.54 to 1.39 is reported, which are reasonable values since the pH of the diluted solutions approach that of the dry ionic liquid.

From Figure 30, one can clearly see the dilution effect. Each dilution step led to a decrease of the current density, since the overall analyte concentration decreased. Except for the first dilution step, the peak current density of the Fe^{2+}/Fe^{3+} couple decreased. This initial increase in peak current density upon dilution might be explained by an effect acting contrary to the dilution. The spiked EAC-1 solution has plenty of dissolved ions drastically increasing the viscosity. By adding dry IL, the viscosity decreases with each step hence increasing ionic mobility (diffusion coefficient). Note that also the hydrogen evolution reaction is affected by the increasing hydrogen sulfate ion concentration, as it is reflected by an increasing current density at the switching potential of -2 V.

Additionally, it can be seen in Figure 30 that the reduction peak potential E_p^{red} of the iron redox peak pair is stronger affected by the dilution than E_p^{ox}. While E_p^{red} changed by +155 mV from 0.563 V in the spiked EAC-1 solution to -0.408 mV in the final dilution step, E_p^{ox} only changed by +14 mV. It was tried to correlate the HSO_4^- concentration in the ionic liquid with the peak potential shift. Therefore the pH value in the aqueous solution was used to determine the HSO_4^- concentration using a pKs value of 1.99 and the same considerations as discussed in Section 3.1.2. The HSO_4^- amount in the aqueous solution and the added IL must be equal and hence the hydrogen sulfate ion concentration in the ionic liquid was determined. However, the calculated hydrogen sulfate ion concentration in the ionic liquid proved to be unrealistically high with values exceeding the maximal theoretical concentration. The reason for this might be due to unknown parameters, like an increased density of the spiked EAC-1 solution which is presumably

significantly increased due to the large amount of dissolved species. Nonetheless, there still is a reasonably good correlation of the calculated hydrogen sulfate concentration and the peak potential shift, as shown in Figure 31.

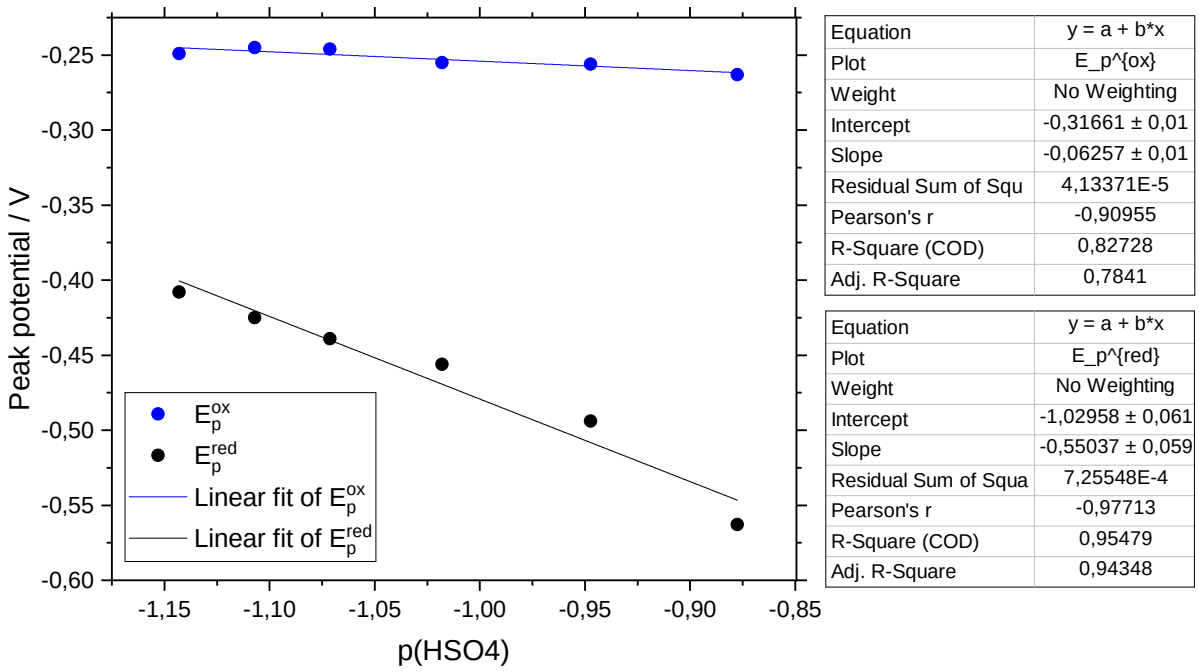

Equation	y = a + b*x
Plot	E_p^{ox}
Weight	No Weighting
Intercept	-0,31661 ± 0,01
Slope	-0,06257 ± 0,01
Residual Sum of Squ	4,13371E-5
Pearson's r	-0,90955
R-Square (COD)	0,82728
Adj. R-Square	0,7841

Equation	y = a + b*x
Plot	E_p^{red}
Weight	No Weighting
Intercept	-1,02958 ± 0,061
Slope	-0,55037 ± 0,059
Residual Sum of Squa	7,25548E-4
Pearson's r	-0,97713
R-Square (COD)	0,95479
Adj. R-Square	0,94348

Figure 31: Correlation of peak potentials from Figure 30 with the negative decadic logarithm of the hydrogen sulfate ion concentration p(HSO_4^-) in the IL.

This experiment confirms the assumption that the acid/base ratio c(HSO_4^-)/c(SO_4^{2-}) is indeed affecting the formation of different Fe ion complexes, which results in the observed potential sift. However, while E_p^{red} is much stronger affected than E_p^{ox}, even the significant shift of +155 mV for E_p^{red} is not enough to explain the large peak shift of +281 mV between the Fe(III) solution and the spiked EAC-1 solution as seen in Figure 27. Hence the acid/base ratio cannot be the only factor influencing the formation of iron complexes.

4 Conclusion

This work presents experimental data concerning the feasibility of an in-situ resource utilization (ISRU) oxygen extraction method, using a lunar regolith simulant and a Brønsted acidic ionic liquid as described by Karr et al. [20]. The used regolith simulant was EAC-1 which is a recently developed lunar mare regolith simulant [7] and the used ionic liquid was 1-ethyl-3-methyliomidazolium hydrogen sulfate ([EMIm][HSO_4]).
As a first step a dissolution strategy was developed and de-ionized water was employed together with the ionic liquid to dissolve EAC-1 at a useful rate. After removing water from the mixture, the total dissolved fraction of EAC-1 amounts to 31.4±1.5 wt.%. By conducting an ICP-OES analysis of the solute, it was found that Mg, Fe, Al, Na and Ca dissolve in major quantities and also small amounts of K, P and Ti are in solution. The key step of this ISRU method is the regeneration the ionic liquid after removal of the produced water by electrochemically plating the metals from the solution at the cathode while oxidizing hydrogen at the anode to replenish the acidity. This work focused on the metal reduction step, since hydrogen oxidation in protic acidic ionic liquids has already been demonstrated before [28, 29].
The electrochemical behavior of the ionic liquid itself and with dissolved EAC-1 was investigated by cyclic voltammetry as the main characterization technique. The electrochemical potential window of the ionic liquid was determined to be at least 2.95 V, if glassy carbon is used as electrode material. It was also determined that this window is highly dependent on the water concentration, with small amounts of 0.22 wt.% already having a measurable effect. Since the ionic liquid electrolyte is Brønsted acidic, the limiting cathodic reaction is the evolution of hydrogen via reduction of hydrogen sulfate ions. Cyclic voltammograms of dissolved EAC-1 show a pronounced peak pair, which was identified to originate from the Fe^{3+}/Fe^{2+} redox couple. It was tried without success to deposit dissolved metals from the EAC-1 solution by conducting potential controlled electrolysis experiments for an extended time at and beyond the cathodic end of the potential window. To better understand the behavior of dissolved iron in [EMIm][HSO_4], model solutions containing certain amounts of Fe^{3+} and Fe^{2+} were prepared and studied in greater detail. It was found that the potential of the Fe^{3+}/Fe^{2+} redox couple somewhat differs between the model solutions and the solution containing regolith simulant EAC-1. In relation to the EAC-1 solution, the Fe^{3+} model solution has a peak potential shifted by +281 mV for the Fe^{3+} reduction, and by +304 mV for the Fe^{2+} oxidation. In an attempt to better understand this peak potential shift, the effect of the hydrogen sulfate ion concentration on the electrochemical behavior was investigated. This investigation revealed that the hydrogen sulfate ion concentration is indeed affecting the electrochem-

ical behavior, whereby the reduction reaction of Fe^{3+} is much stronger affected than the Fe^{2+} oxidation. However, even the peak potential shift of the Fe^{3+} reduction caused by varying the hydrogen sulfate ion concentration is not large enough to explain the total peak potential shift between the regolith solution and the neat iron solution. Thus other factors caused by the presence of dissolved EAC-1 must play a critical role in determining the iron reduction and oxidation behavior, like the formation of different iron complex coordinations, different diffusion coefficients of Fe^{3+} and Fe^{2+} and/or dissimilar Fe^{3+} to Fe^{2+} ratios.

Moreover, the cyclic voltammograms of the model solutions and the regolith simulant solution did not show a pronounced and consistent metal deposition reaction. A distinct reduction process is observed towards the cathodic end of the potential window in the Fe^{3+} solution, yet this is difficult to reproduce and heavily dependent on the previous sequence of experiments. We hypothesize that this behavior is caused by the reduction of residual water, leading to iron hydroxide formation at the surface of the electrode and causing a temporal electrode passivation. This passivation process might also be one of the reasons why the potential controlled electrolysis experiments aimed at iron deposition were unsuccessful.

Overall, this work demonstrated that regolith simulant dissolution is possible in a Brønsted acidic ionic liquid and delivers a first electrochemical characterization of the resulting electrolyte solution. While this oxygen extraction method in theory poses an elegant way of electrolyzing regolith at low temperatures, regenerating the ionic liquid electrolyte remains the major practical hurdle in this process sequence. A better understanding of the ion/electrolyte interactions in this highly complex medium could possibly solve the metal deposition problem and hence a successful ionic liquid recovery might be achieved.

References

(1) Lunar Samples Lunar and Planetary Institute (11th January 2021), `https://www.lpi.usra.edu/lunar/samples/`.

(2) Luna 16 NASA Space Science Data Coordinated Archive (11th January 2021), `https://nssdc.gsfc.nasa.gov/nmc/spacecraft/display.action?id=1970-072A`.

(3) Luna 20 NASA Space Science Data Coordinated Archive (11th January 2021), `https://nssdc.gsfc.nasa.gov/nmc/spacecraft/display.action?id=1972-007A`.

(4) Luna 24 NASA Space Science Data Coordinated Archive (11th January 2021), `https://nssdc.gsfc.nasa.gov/nmc/spacecraft/display.action?id=1976-081A`.

(5) Schreiner, S. S.; Dominguez, J. A.; Sibille, L.; Hoffman, J. A. *Advances in Space Research* **2016**, *57*, 1209–1222.

(6) Taylor, L. A.; Pieters, C. M.; Britt, D. *Planetary and Space Science* **2016**, *126*, 1–7.

(7) Engelschiøn, V.; Eriksson, S.; Cowley, A.; Fateri, M.; Meurisse, A.; Kueppers, U.; Sperl, M. *Scientific Reports* **2020**, *10*, 1–9.

(8) Stoeser, D.; Rickman, D.; Wilson, S. *Design and specifications for the highland regolith prototype simulants NU-LHT-1M and-2M*; tech. rep.; NASA Marshall Space Flight Center; Huntsville, AL, United States, 2011.

(9) Taylor, L. A.; Carrier, W. D. *AIAA Journal* **1992**, *30*, 2858–2863.

(10) Schlüter, L.; Cowley, A. *Planetary and Space Science* **2020**, *181*, 104753.

(11) Gibson, M. A.; Knudsen, C. W.; Brueneman, D. J.; Allen, C. C.; Kanamori, H.; McKay, D. S. *Journal of Geophysical Research: Planets* **1994**, *99*, 10887–10897.

(12) Sanders, G. B.; Larson, W. E. *Journal of Aerospace Engineering* **2013**, *26*, 5–17.

(13) Senior, C. In *Space Programs and Technologies Conference*, 1992.

(14) Colozza, A. J. *Analysis of lunar regolith thermal energy storage*; tech. rep.; NASA Contractor Report 189073, 1991.

(15) Lomax, B. A.; Conti, M.; Khan, N.; Bennett, N. S.; Ganin, A. Y.; Symes, M. D. *Planetary and Space Science* **2020**, *180*, 104748.

(16) Gordon, C. M.; Muldoon, M. J.; Wagner, M.; Hilgers, C.; Davis Jr., J. H.; Wasserscheid, P. In *Ionic Liquids in Synthesis*; John Wiley & Sons, Ltd: 2007; Chapter 2, pp 7–55.

(17) Hallett, J. P.; Welton, T. *Chemical reviews* **2011**, *111*, 3508–3576.

(18) Beyersdorff, T.; Schubert, T. J. S.; Welz-Biermann, U.; Pitner, W.; Abbott, A. P.; McKenzie, K. J.; Ryder, K. S. In *Electrodeposition from Ionic Liquids*; John Wiley & Sons, Ltd: 2017; Chapter 2, pp 17–53.

(19) Paley, M. S.; Karr, L. J.; Curreri, P.; Marone, M. In *Space, Propulsion and Energy Sciences International Forum*, 2009, pp 1–20.

(20) Karr, L.; Curreri, P.; Thornton, G.; Depew, K.; Vankeuren, J.; Regelman, M.; Fox, E.; Marone, M.; Donovan, D.; Paley, M. In *2018 AIAA SPACE and Astronautics Forum and Exposition*, 2018, p 5291.

(21) Bhatt, A. I.; Snook, G. A. In *Handbook of Reference Electrodes*, Inzelt, G., Lewenstam, A., Scholz, F., Eds.; Springer Berlin Heidelberg: Berlin, Heidelberg, 2013, pp 189–227.

(22) Caclium Oxide, ILO International Chemical Safety Cards (ICSC), `https://www.ilo.org/dyn/icsc/showcard.display?p_version=2&p_card_id=0409`.

(23) Sodium Oxide, ILO International Chemical Safety Cards (ICSC), `https://www.ilo.org/dyn/icsc/showcard.display?p_version=2&p_card_id=1653`.

(24) Potassium oxide, NOAA Cameo Chemicals, `https://cameochemicals.noaa.gov/chemical/4322`.

(25) Phosphorus pentoxide, ILO International Chemical Safety Cards (ICSC), `https://www.ilo.org/dyn/icsc/showcard.display?p_version=2&p_card_id=0545`.

(26) Jencks, W. (11th January 2021), `https://organicchemistrydata.org/hansreich/resources/pka/pka_data/pka-compilation-williams.pdf`.

(27) Calcium sulfate dihydrate, ILO International Chemical Safety Cards (ICSC), `https://www.ilo.org/dyn/icsc/showcard.display?p_version=2&p_card_id=1734`.

(28) Johnson, L.; Ejigu, A.; Licence, P.; Walsh, D. A. *The Journal of Physical Chemistry C* **2012**, *116*, 18048–18056.

(29) Silvester, D. S.; Ward, K. R.; Aldous, L.; Hardacre, C.; Compton, R. G. *Journal of Electroanalytical Chemistry* **2008**, *618*, 53–60.

(30) Matsumoto, H. In *Electrochemical Aspects of Ionic Liquids*; John Wiley & Sons, Ltd: 2011; Chapter 4, pp 43–63.

(31) Trasatti, S.; Petrii, O. A. *Journal of Electroanalytical Chemistry* **1992**, *327*, 353–376.

(32) Bard, A. J.; Faulkner, L. R., *Electrochemical Methods: Fundamentals and Applications*, second edition; John Wiley & Sons, Inc.: 2001.

(33) Snook, G.; Best, A.; Pandolfo, A.; Hollenkamp, A. *Electrochemistry Communications* **2006**, *8*, 1405–1411.

(34) Zhang, Z.; Kitada, A.; Fukami, K.; Yao, Z.; Murase, K. *Electrochimica Acta* **2020**, *348*, 136289.

(35) Elgrishi, N.; Rountree, K. J.; McCarthy, B. D.; Rountree, E. S.; Eisenhart, T. T.; Dempsey, J. L. *Journal of Chemical Education* **2018**, *95*, 197–206.

List of Figures

1 Picture of the moon as seen from earth. Dark patches are the mare regions, brighter areas are the highland regions (Photo by Mike Petrucci on Unspash). 1
2 Examples of commonly used cation structures for the synthesis of ionic liquids. [18] 4
3 Examples of commonly used anions for the synthesis of ionic liquids. [18] . 4
4 Chemical structure of the protic acidic ionic liquid 1-ethyl-3-methylimidazolium hydrogen sulfate ([EMIm][HSO_4]) as used in this work and by Karr et al. [20] 5
5 (a) Drawing illustrating the experimental setup for EAC-1 dissolution; (b) picture of the EAC-1 dissolution setup. 7
6 (a) Drawing illustrating the vacuum filtration setup; (b) picture of the vacuum filtration setup. 8
7 Picture of the setup used to dry the ionic liquid mixture. In this picture a glass cell and a round bottom flask are connected to the vacuum line. The glass cell is heated with a thermostat, the round bottom flask with an oil bath. 9
8 (a) Drawing illustrating the glass Haber Luggin capillary reference electrode setup; (b) Picture of disassembled reference electrode; (c) picture of assembled reference electrode. 10
9 (a) Drawing of the electrochemical glass cell; (b) picture of an empty electrochemical glass cell. 11
10 Typical electrochemical equipment, which is inserted into the 5-joint glass cell 11
11 (a) Drawing illustrating a close up view of the electrode arrangement inside the glass cell filled with electrolyte; (b) close-up picture of the electrode arrangement in the electrochemical glass cell. 12
12 (a) Picture showing the measurement setup inside a fume hood; (b) Close up picture of the electrochemical glass cell inside the faraday cage connected to the potentiostat. 13
13 Graph relating the dissolved fraction of EAC-1 to the amount of IL added to 30 ml water. 15
14 Graph showing the measured and calculated pH dependence of the aqueous [EMIm][HSO_4] solution in relation to the ionic liquid amount per one gram of EAC-1. 18

15 Column chart showing the molar concentration of dissolved metal species in the aqueous solution depending on the [EMIm][HSO_4] concentration. . . 20
16 Column chart showing the relative amount of dissolved oxides in the aqueous [EMIm][HSO_4] solution. 21
17 Dissolved fraction of EAC-1 obtained from gravimetric data and from metal ion concentrations measured with ICP-OES. 22
18 Cyclic voltammograms recorded in [EMIm][HSO_4] with a sweep rate of 100 mV/s, at 70 °C with 3 mm diameter disk electrodes of different materials. 24
19 Cyclic voltammograms recorded with a sweep rate of 100 mV/s, at 70 °C in [EMIm][HSO_4] with a 3 mm diameter glassy carbon disc electrode. . . . 25
20 Cyclic voltammograms of dissolved EAC-1 and dried ionic liquid recorded with a sweep rate of 100 mV/s, at 70 °C with a 3 mm diameter glassy carbon disc electrode. 27
21 Current-time curves of three potential-controlled electrolyses of EAC-1 dissolved in [EMIm][HSO_4] at three different potentials. The sample names, electrode materials was well as the step potentials are noted in the legend. 30
22 Scanning electron microscope images of three electrodes used in the potential-controlled electrolyses in Figure 21. All images were recorded with a secondary electron detector. The sample name is listed at the top left of each picture. 31
23 SEM picture of sample A of a region with high contrast recorded with the SE (left) and the BSE detector (right). 32
24 SEM picture highlighting the five EDX measuring spots in the high contrast region of sample A. 32
25 EDX spectra in the high contrast region on the surface of sample A. 33
26 Cyclic voltammograms of the EAC-1 solution and said solution spiked with iron(III) sulfate. The cyclic voltammograms were recorded with a sweep rate of 100 mV/s, at 70 °C with a 3 mm diameter glassy carbon disc electrode. 35
27 Cyclic voltammograms of the spiked EAC-1 solution and the iron(III) sulfate solution. The cyclic voltammograms were recorded with a sweep rate of 100 mV/s, at 70 °C with a 3 mm diameter glassy carbon disc electrode. . 38

28 Cyclic voltammograms of the iron(III) sulfate solution. The CVs were recorded in succession during a multi cycle experiment using the same experiment parameters. Up to 30 CVs were recorded and the scan number can be seen in the top left corner of each graph. The cyclic voltammograms were recorded with a sweep rate of 100 mV/s, at 70 °C with a 3 mm diameter glassy carbon disc electrode. The start potential (SP) of the experiment was 0.120 V. 40
29 Cyclic voltammograms in the iron(II) sulfate solution. The CVs were recorded in succession during a multi cycle experiment using the same experiment parameters. The cycle number can be seen in the top left corner of each graph. Experiments were carried out with a sweep rate of 100 mV/s, at 70 °C with a 3 mm diameter glassy carbon disc electrode. The start potential (SP) of the experiment, which was equal to the OCP, was -0.320 V. 42
30 Cyclic voltammograms of Fe(III)-spiked EAC-1 solution (see Section 3.2.4) and of several dilutions of said solution. The cyclic voltammograms were recorded with a sweep rate of 100 mV/s, at 70 °C with a 3 mm diameter glassy carbon disc electrode. The black arrow indicates the sweep direction which remained unchanged for each measurement. 44
31 Correlation of peak potentials from Figure 30 with the negative decadic logarithm of the hydrogen sulfate ion concentration p(HSO_4^-) in the IL. . 46
A1 Graph relating the pH value in the aqueous [EMIm][HSO_4] and EAC-1 suspension before and after the dissolution step to the gravimetric dissolution data. 57
A2 Certificate of analysis from proionic of [EMIm][HSO_4]. 58
A3 SEM pictures of sample B recorded with the SE and BSE detector. 58
A4 SEM pictures of sample C recorded with the SE and BSE detector. 59
A5 SEM pictures of sample C recorded with a SE detector. 59

List of Tables

1 Oxide fractions in lunar regolith types [8] and EAC-1 simulant [7]. EAC-1 was analyzed with EDX and only fractions $\geq$ 0.5 wt.% are displayed. . . . 2
2 List of all chemicals used in this work 6
3 Parameters of dissolution experiments based on 1 g of EAC-1 regolith simulant material. 7

4 Data used to calculate the pH value of the aqueous suspension before the dissolution of EAC-1. 17
5 Volume of aqueous liquid after filtration 19
6 Standard electrode potentials of substances found in EAC-1 in aqueous solution at 25°C in V vs. SHE [32] and transformed to V vs. Ag/Ag^+ [33]. 28
7 Results of the EDX analysis at the high contrast region of sample A at five measuring spots. 34
8 Cyclic voltammetric data and OCP value of the measurements in Figure 26 35
9 Cyclic voltammetric data from Fe(III) solution experiment. 38
10 Cyclic voltammetric data from successively recorded cycles of the Fe^{2+}/Fe^{3+} peak pair as seen in Figure 28. 40
11 Cyclic voltammetric data from successively recorded cycles of the iron(II) solution as seen in Figure 29. 43
12 Cyclic voltammetric data from Figure 30. 45
A1 Dissolution results of EAC-1 in aqueous [EMIm][HSO_4] solution. 56
A2 All uncorrected ICP-OES data as received. 57

Appendix

Table A1: Dissolution results of EAC-1 in aqueous [EMIm][HSO_4] solution.

m(IL) [g]	pH before dissolution	pH after dissolution	Dissolution [wt.%]
0		9.02	12
1	1.78	2.58	16
2.03	1.25	2.08	20
3.05	1.2	1.64	20
4.09	1.1	1.49	17
4.99	0.97	1.21	18
5.98	1.03		26
6.22	1.13		29
6.22	1.09	1.12	30
7.00			33
7.00	1.1	1.16	30
7.01			31.25
10	0.75	1.17	32

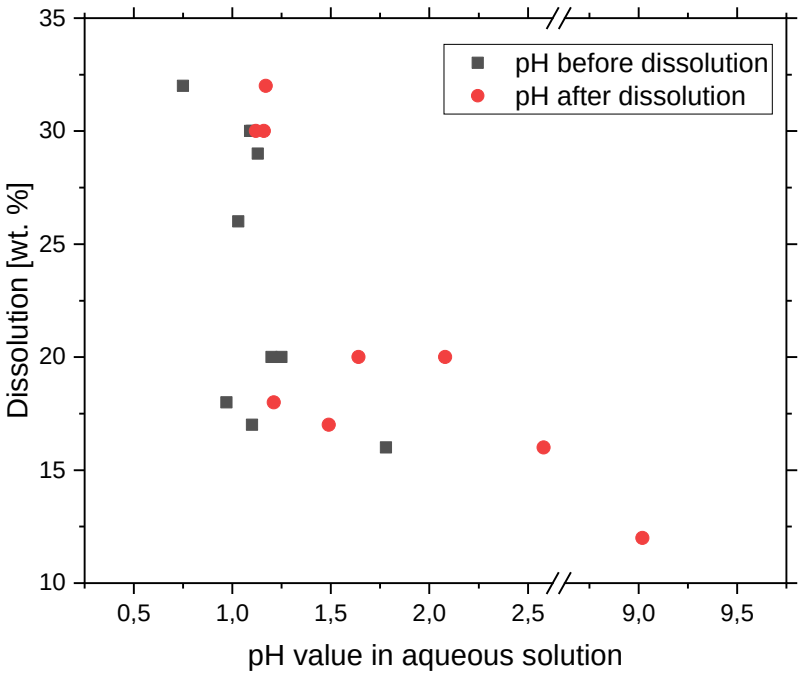

Figure A1: Graph relating the pH value in the aqueous [EMIm][HSO_4] and EAC-1 suspension before and after the dissolution step to the gravimetric dissolution data.

Table A2: All uncorrected ICP-OES data as received.

	m(EMIM HSO4)/m(EAC-1) in aqueous solution [g/g]						
Metal species	0	1	2	3	4	5	6
Al (396.152 nm)	<LOQ (0.1 mg/L)	13.4 ± 0.5 mg/L	500 ± 20 mg/L	500 ± 20 mg/L	710 ± 30 mg/L	630 ± 20 mg/L	1520 ± 60 mg/L
Ca (396.847 nm)	340 ± 10 mg/L	224 ± 9 mg/L	370 ± 10 mg/L	330 ± 10 mg/L	390 ± 10 mg/L	320 ± 10 mg/L	140 ± 6 mg/L
Fe (259.941 nm)	<LOQ (0.2 mg/L)	330 ± 10 mg/L	760 ± 30 mg/L	730 ± 30 mg/L	970 ± 40 mg/L	860 ± 30 mg/L	2500 ± 100 mg/L
K (766.491 nm)	7.7 ± 0.3 mg/L	18.9 ± 0.8 mg/L	111 ± 4 mg/L	101 ± 4 mg/L	130 ± 5 mg/L	109 ± 4 mg/L	280 ± 10 mg/L
Mg (285.213 nm)	3.9 ± 0.2 mg/L	630 ± 30 mg/L	1200 ± 50 mg/L	1100 ± 50 mg/L	1400 ± 60 mg/L	1200 ± 50 mg/L	3700 ± 100 mg/L
Mn (257.611 nm)	<LOQ (0.1 mg/L)	12.6 ± 0.5 mg/L	20 ± 1 mg/L	18.7 ± 0.7 mg/L	26 ± 1 mg/L	24 ± 1 mg/L	57 ± 2 mg/L
Na (330.237 nm)	41 ± 2 mg/L	219 ± 9 mg/L	339 ± 10 mg/L	300 ± 10 mg/L	380 ± 20 mg/L	320 ± 10 mg/L	940 ± 40 mg/L
P (177.495 nm)	<LOQ (5 mg/L)	<LOQ (5 mg/L)	58 ± 2 mg/L	56 ± 2 mg/L	74 ± 3 mg/L	56 ± 2 mg/L	160 ± 6 mg/L
Ti (334.941 nm)	<LOQ (0.1 mg/L)	<LOQ (0.1 mg/L)	1.5 ± 0.1 mg/L	2.4 ± 0.1 mg/L	11.0 ± 0.4 mg/L	14.5 ± 0.6 mg/L	77 ± 3 mg/L

proionic

proionic GmbH, Parkring 18/ H/1, A-8074 Grambach/Graz
Tel.: +43 316 4009 4200; office@proionic.com

Certificate of Analysis

Product name	***1-Ethyl-3-methylimidazolium hydrogensulfate***
PI product number	00131.3000
Purity	purum
Molecular formula	$C_6H_{12}N_2O_4S$
Molecular weight	208.24 g*mol^{-1}
CAS Number	412009-61-1
LOT Number	27PI442_2

CHARACTERISTIC	***SPEZIFICATION***	***LOT RESULT***
assay $EMIM^+$, *HPLC*	≥ 98.0%w	98.57 ± 0.09 %w
assay HSO_4^-, *NaOH titration*	≥ 98.0%w	98.13 ± 0.12 %w
halides, *IC*	< 50 ppm_w	< 10 ppm_w
assay H_2O, *Karl Fischer titration*	< 0.5%w	0.20 ± 0,01%w
aspect, *acc. to Ph. Eur. 5.0*	turbid viscous liquid	turbid viscous liquid
color, *acc. to Ph. Eur. 5.0*	lightly yellow	lightly yellow

QC Release Date 26. February 2020

Quality Executive

Quality Assurance

proionic PI.CoA.00131.3000_01

Figure A2: Certificate of analysis from proionic of [EMIm][HSO_4].

Figure A3: SEM pictures of sample B recorded with the SE and BSE detector.

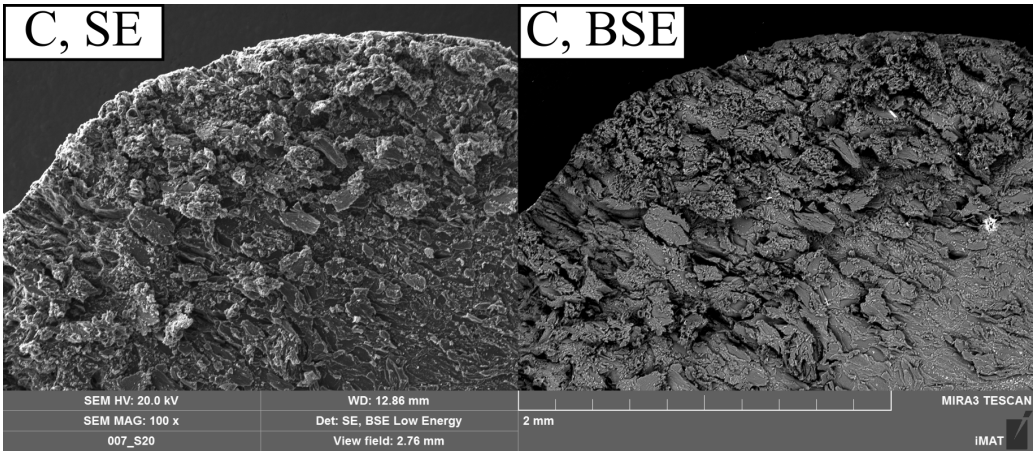

Figure A4: SEM pictures of sample C recorded with the SE and BSE detector.

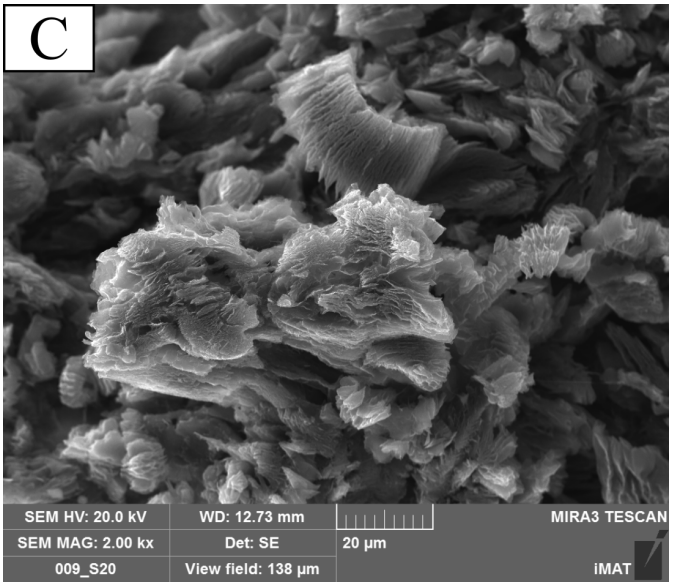

Figure A5: SEM pictures of sample C recorded with a SE detector.